

# Galaxy formation physics behind bar formation: View from cosmological hydrodynamic simulations

Yetli Rosas-Guevara<sup>1\*</sup>, Silvia Bonoli<sup>1,2</sup>, Ewald Puchwein<sup>3</sup>, Massimo Dotti<sup>4,5,6</sup>, and Sergio Contreras<sup>1</sup>

<sup>1</sup> Donostia International Physics Centre (DIPC), Paseo Manuel de Lardizabal 4, 20018 Donostia-San Sebastian, Spain

<sup>2</sup> IKERBASQUE, Basque Foundation for Science, E-48013, Bilbao, Spain

<sup>3</sup> Leibniz-Institut für Astrophysik Potsdam, An der Sternwarte 16, 14482 Potsdam, Germany

<sup>4</sup> Dipartimento di Fisica G. Occhialini, Università di Milano-Bicocca, Piazza della Scienza 3, IT-20126 Milano, Italy

<sup>5</sup> INFN, Sezione di Milano-Bicocca, Piazza della Scienza 3, IT-20126 Milano, Italy

<sup>6</sup> INAF, Osservatorio Astronomico di Brera, Via E. Bianchi 46, I-23807, Merate, Italy

Received September 15, 1996; accepted March 16, 1997

## ABSTRACT

We present a suite of zoom-in cosmological simulations of Milky Way-like galaxies with a prominent disc component and a strong bar in their centre, based on a subsample of barred galaxies from the TNG50 magneto-hydrodynamic simulation. We modify the physical models that regulate star formation, namely, supernova feedback and black hole quasar feedback, to examine how they affect the disc and bar formation. We find that the morphology remains consistent in all the galaxies that develop a massive stellar disc ( $> 10^{10} M_{\odot}$ ), which is dominant in comparison with the bulge mass. The black hole quasar feedback models used in this work do not affect bar formation, although they can affect the properties of the bar. The energy released by the supernovae causes a delay in the time of bar formation and, in models with strong feedback, stops bar formation. This could be understood since supernova feedback affects the assembly of the disc and bulge and their structural properties, such as the mass content, size, and radial velocity dispersion. We compared our predictions to three bar instability criteria proposed in the literature. We find that galaxies with varying supernovae and black hole quasar feedback satisfy these criteria at the moment of bar formation, except in extreme cases where the galaxy does not have or has weak supernova feedback, where for some galaxies, they fail to predict the existence (or no existence) of bars. Our findings provide insights into the physical process behind bar formation while putting constraints on the analytic prescriptions that predict bar formation.

**Key words.** Galaxies: evolution, Galaxies: structure, Galaxies: spiral, Methods: numerical

## 1. Introduction

Galactic bars are elongated structures of stars, gas, and dust that extend from the centres of many disk galaxies, including the Milky Way. They are common features observed in spiral galaxies across the Universe; at least two-thirds of the local spirals have a bar (e.g., Sellwood & Wilkinson 1993; Masters et al. 2011; Gavazzi et al. 2015). Bars are also observed in high redshift galaxies, although the fraction is still uncertain (Guo et al. 2023; Le Conte et al. 2023; Guo et al. 2024). These bars form due to gravitational instabilities within the galactic disc, which lead to the redistribution of angular momentum (e.g., Athanassoula & Misiriotis 2002; Athanassoula 2003; Debattista et al. 2006; Sellwood 2012). This process could funnel interstellar gas towards the galactic centre, often resulting in an enhanced central bulge and increased star formation activity in the core regions (e.g. Spinoso et al. 2017; Donohoe-Keyes, et al. 2019; George et al. 2019). Stellar bars play an active role in the secular evolution of galaxies by redistributing mass and angular momentum, thereby influencing the overall morphology and dynamics of the galaxy.

One open question is which disc galaxies form a galactic bar and when. Many studies have investigated the conditions of a disc to form a bar since the early 60s, with the seminal work of Toomre (1964), which emphasizes the importance of random stellar motions in maintaining the stability of galactic disks and

provides a framework for understanding the dynamics of stellar systems. Toomre (1964) proposed a dimensionless parameter, the Toomre parameter  $Q_T$ , that is employed to evaluate the stability of a differentially rotating disc:

$$Q_T = \frac{\kappa \sigma_R}{3.36 G \Sigma}, \quad (1)$$

where  $\kappa$  and  $\sigma_R$  denote the epicyclic frequency and velocity dispersion of the stars in the radial direction, respectively;  $\Sigma$  denotes the face-on stellar surface density profile; and  $G$  denotes the gravitational constant. The disc's stability in response to axisymmetric density perturbations is determined by the Toomre parameter. If  $Q_T < 1$ , the disc is unstable. Ostriker & Peebles (1973) proposed that the ratio between the kinetic energy of rotation to the total gravitational energy of the galaxy has to be  $\lesssim 0.14$  to be stable. In addition, Efstathiou, Lake & Negroponte 1982, (ELN), by studying models with exponential surface density profiles and flat rotation curves at large radii, investigated the formation of bars. The authors find that a critical criterion for stability in bar-like modes in disc galaxies is given by

$$\epsilon_{\text{ELN}} \equiv v_{\text{Max}} / (M_{\text{disc}} G / r_{\text{disc}})^{1/2} \geq 1.1, \quad (2)$$

where  $v_{\text{Max}}$  is the maximum rotational velocity of the system,  $r_{\text{disc}}$  corresponds to the scale length of the exponential disc and  $M_{\text{disc}}$  is the total disc mass. They also explore the role of a hot halo component in increasing this ratio to stabilise the galaxy

\* email: yetli.rosas@dipc.org

against bar formation. The study highlights the importance of balancing parameters like rotational velocity, scale length, and total disc mass to maintain stability in disc galaxies. Izquierdo-Villalba et al. (2022) have investigated if the ELN criterion is satisfied for massive galaxies with strong bars in the TNG100 and TNG50 simulations. They find that more than 70 per cent of the barred galaxies satisfied the ELN criterion, while in galaxies that do not satisfy the criterion, it is because the bar formation is triggered by a tidal interaction rather than secular evolution. This criterion was revised by Mo, Mao, & White 1998, (MMW) with a focus on more fundamental properties, including the spin parameter ( $\lambda$ ), the stellar disc mass fraction ( $m_{\text{disc}} = M_{\text{disc}}/M_h$ ), and the angular momentum of the disc ( $J_{\text{disc}}$ ) and halo ( $J_h$ ). The authors found in their disc and halo profile that the discs are stable if  $\lambda_{\text{MMW}} > \lambda_{\text{crit}}$  where  $\lambda_{\text{MMW}}$  is defined as

$$\lambda_{\text{MMW}} \equiv \lambda \frac{J_{\text{disc}}}{J_h} \frac{M_{\text{disc}}}{M_h} \geq \lambda_{\text{crit}} = \sqrt{2} \epsilon_{\text{ELN}}^2 m_{\text{disc}} f_c^{1/2} f_R^{-1} f_V^{-2}, \quad (3)$$

where  $\lambda = |J_h| / (\sqrt{2} M_{200} V_{200} r_{200})$  where  $J_h$  is the angular momentum evaluated at  $r_{200}$  (Bullock et al. 2001). The functions  $f_c, f_R, f_V$  weakly depend on the profile models of the disc and halo and seen in Fig. 3 by Mo, Mao, & White 1998, (MMW). Because of this, a useful but rough approximation is that  $\lambda_{\text{MMW}} > m_{\text{disc}}$  that could be translated into  $\lambda \frac{J_{\text{disc}}}{J_h} \frac{M_{\text{disc}}}{M_h} > 1$  where  $j_{\text{disc}}$  and  $j_h$  are the specific angular momentum of the disc and halo.

Although these criteria are widely used to predict bar instabilities in galaxy formation models, some theoretical and observational studies have shown that bar formation could be more complex and that other ingredients may affect bar evolution. For instance, Athanassoula (2008) discusses that ELN does not take into account the (stabilising) effect of the disc velocity dispersion or the central concentration. Ghosh et al. (2023) found that using different contributions of the thick discs, some of their galaxies do not satisfy the ELN criterion. Romeo, Agertz, & Renaud (2023) found that for more diverse barred/unbarred disc galaxy samples (the galaxies of types S0–BCD from the Spitzer Photometry and Accurate Rotation Curves' sample (SPARC) and galaxies of type Im from the Local Irregulars That Trace Luminosity Extremes The HI Nearby Galaxy Survey (LITTLE THINGS), some criteria could not be applied for all the diversity of galaxies found in the local Universe. In addition, other components, such as the bulge, could avoid the formation of a bar. Saha & Elmegreen (2018) show that disc galaxies with a bulge denser than their disc can prevent bar formation even though the disc is maximal or unstable to bar instabilities. This is due to the rapid loss of angular momentum and rapid heating in the centre of initially strong bar and spiral arms. Also, high-rotating dark matter haloes could prevent the growth of bar instabilities. Saha & Naab (2013) also show that bar formation is favoured in haloes corotating with the disc with a dark matter spin parameter ( $\lambda_{\text{DM}}$ ) in the range of 0 and 0.07. However, Long, Shlosman, & Heller (2014) have shown that the bar growth is halted in haloes with larger spins ( $\lambda_{\text{DM}} \gtrsim 0.03$ ). Collier, Shlosman, & Heller (2018) suggested that not only the spin parameter but also the shape of the dark matter halo is important to the evolution of bars. Yurin & Springel (2015) have considered the stability of discs by inserting already formed stellar discs in haloes using the Aquarius simulation project that consists of zoom-in, dark matter-only simulations. These authors found that the 3-D shape of the dark matter halo could affect the stability of the disc. Independently of the results, all these studies show the importance of the angular momentum exchange between the dark matter and the stellar

components in the formation of a bar (see also Sheth et al. 2012; Athanassoula et al. 2013).

The bulge and disc structural properties are related to the formation of galactic bars and are the result of the formation history of the galaxy in the first place (Mo, Mao, & White 1998; Rosito et al. 2019; Bi, Shlosman, & Romano-Díaz 2022a; Joshi et al. 2024). One crucial driver that could influence the morphology of galaxies since early times is star formation feedback and AGN (Active Galactic Nuclei) feedback. Supernova (SN) feedback refers to the impact of supernova explosions on the interstellar medium (ISM). Massive stars end their lives in supernova explosions, releasing vast amounts of energy, radiation, and heavy elements. This feedback process has several critical effects on the ISM: it injects energy, creating shock waves that can compress or disperse gas clouds; it enriches the ISM with heavy elements necessary for new star formation; and it regulates the star formation rate by preventing runaway star formation that could deplete the galaxy gas reservoir. AGN feedback is powered by the accretion of gas into the supermassive black holes that are thought to be located in the centres of all (sufficiently large) galaxies and has been proposed to mostly affect star formation in massive galaxies (Springel et al. 2005; Bower et al. 2006; Croton et al. 2006). Both SN and AGN feedback are critical processes in all the galaxy formation models today (Springel et al. 2005; Bower et al. 2006; Croton et al. 2006). Both processes inject energy and momentum into the ISM, potentially influencing the star formation and regulating the galaxy build-up and, subsequently, the bar formation. In particular, SN feedback has been demonstrated to be efficient in the accumulation of central low angular momentum gas, allowing for the build-up of cold discs with flat rotation curves comparable with observations Navarro & Benz (1991).

Barred galaxies have started to be explored in a fully cosmological context recently, thanks to high-resolution zoom-in simulations (e.g., Kraljic et al. 2012; Scannapieco & Athanassoula 2012; Bonoli et al. 2016). In particular, Bonoli et al. (2016) present a zoom-in simulation of a Milky Way-type galaxy, *ErisBH*, a sibling of the *Eris* simulation (Guedes et al. 2011), but with black hole (BH) subgrid physics included. Bonoli et al. (2016) and Spinoso et al. (2017) find that the simulated galaxy forms a strong bar below  $z \sim 1$ , and the authors point out that the disc in the simulation is more prone to instabilities compared to the original *Eris*, possibly because of early AGN feedback affecting the central part of the galaxy. Zana et al. (2019), studying a larger suite of *Eris*, highlights the effects of the feedback processes on the formation time and final properties of the bar. Recently, Fragkoudi et al. (2020, 2024) have studied barred galaxy formation in the Auriga suite, which consists of high-resolution, magnetohydrodynamical cosmological zoom-in simulations of galaxy formation (Grand et al. 2017). The authors find that the simulated galaxies that can reproduce many chemodynamical properties of the stellar populations seen in the Milky-way bulge have quiet merger histories. Auriga simulations have also been employed by Irodou et al. (2022) to determine that AGN feedback can influence the final properties of a bar, but not its formation. The formation of bars in high-redshift counterpart galaxies of the local spiral galaxies formed in dense environments and with two distinct SN feedback subgrid models has been investigated by Bi, Shlosman, & Romano-Díaz (2022b) using high-resolution zoom-in simulations. The authors find that the properties and evolution of galactic bars are significantly impacted by the varying SN feedback. These changes are associated with the interactions and cold accretion processes, which were influenced by the type of feedback implemented.

With cosmological hydrodynamic simulations (Vogelsberger et al. 2014a; Schaye et al. 2015; Pillepich et al., 2018b; Nelson et al. 2018, see also the recent review of Vogelsberger et al. 2020a; Crain et al. 2023), it has been possible to follow the formation and evolution of the barred galaxy population in a cosmological context and with a significant statistical sample. Analysing the EAGLE simulation, Algorry et al. (2017) find that bars slow down quickly as they evolve, expanding the inner parts of the dark matter halo. Rosas-Guevara et al. (2020, 2022) study massive barred disc galaxies at  $z = 0$  in the TNG100 and TNG50 simulation (see also Peschken & Lokas 2019; Zhao et al. 2020; Zhou et al. 2020 for Illustris and IllustrisTNG), finding that barred galaxies are less star-forming and more gas poor than unbarred galaxies. Following the evolution of barred galaxies back in time, Rosas-Guevara et al. (2020) find that these objects assembled most of their disc components before bar formation and at earlier times than unbarred galaxies (see also Izquierdo-Villalba et al. 2022).

Even though these simulations have shown the possibility of understanding the evolution and formation of bars in a cosmological context, there are many complex galaxy formation processes that are taking place, and it is difficult to disentangle all the relevant processes. Taking advantage of previous works, we perform zoom-in simulations of six Milky Way-like galaxies from the TNG50 simulations. These galaxies have a stable galactic bar at  $z = 0$  and formed between  $z = 3$  and  $z = 1.5$  (more than 8 billion years ago) and with quiet merger histories and isolated haloes. These zoom-in simulations are run with the AREPO code (Springel 2010) and similar initial conditions as the original TNG50 simulation (Pillepich et al. 2019; Nelson et al. 2019b) in the sense that the large-scale tidal field is very similar, but only the galaxy region simulated with the same resolution as TNG50. Our primary goal is to study the interplay of galaxy formation physics with the formation and evolution of galactic bars. For that, we use the same galaxy formation physics except for variations in the supernova and AGN feedback models to try to identify the specific impacts of these feedback channels. We also explore how these variations impact different bar instability criteria used in the field: the Toomre 1964, and Efstathiou, Lake & Negroponte 1982, (ELN), and Mo, Mao, & White 1998, (MMW) criteria.

The paper is structured as follows. In section 2, we introduce our selection of the disc galaxies and the methodology for identifying a bar and dynamics components, as well as give a brief overview of the supernova and AGN feedback subgrid physics of the TNG50 and their variations used here. In section 3, we study the redshift evolution of their bars and their host galaxy components. We study the criteria of bar instability and how they are affected by the different galaxy formation models in section 4. Finally, in sections 5 & 6, we discuss and summarise our findings, respectively.

## 2. Methodology

In this section, we describe the object selection criteria, the generation of the initial conditions, and the TNG galaxy formation model. We especially describe the variations of the galaxy formation model. This project accounts for 42 resimulations, with six haloes, each with seven different variations of the galaxy formation model. These simulations were performed with the moving-mesh AREPO code (Springel 2010), combining Tree-PM and Godunov/finite volume methods to discretize space. The quasi-Lagrangian scheme is second-order in space and time.

The cosmology parameters adopted are from the Planck Collaboration (2016) Cosmology:  $\Omega_\Lambda = 0.6911$ ,  $\Omega_m = 0.3089$ ,  $\Omega_b = 0.0486$ ,  $\sigma_8 = 0.8159$ ,  $h = 0.6774$ , and  $n_s = 0.9667$  where  $\Omega_\Lambda$ ,  $\Omega_m$ , and  $\Omega_b$  are the average densities of dark energy, matter and baryonic matter in units of the critical density at  $z = 0$ ,  $\sigma_8$  is the square root of the linear variance,  $h$  is the Hubble parameter ( $H_0 \equiv h 100 \text{ km s}^{-1}$ ) and,  $n_s$  is the scalar power-law index of the power spectrum of primordial adiabatic perturbations.

The suite of zoom-in simulations has a similar resolution to the TNG50 simulation, whose particle mass resolution is  $4.5 \times 10^5 M_\odot$  for dark matter particles, whereas the mean cell mass resolution is  $8.5 \times 10^4 M_\odot$  for gas. A comparable initial mass is passed down to stellar particles, which subsequently lose mass through stellar evolution. The spatial resolution, i.e. the gravitational softening, for collisionless particles (dark matter and stellar particles) is 575 comoving pc down to  $z = 1$ , after which it remains constant at 288 pc in physical units down to  $z = 0$ . In the case of the gas component, the gravitational softening is adaptive and based on the effective cell radius, down to a minimum value of 72 pc in physical units, which is imposed at all times.

Galaxies and their haloes are identified as bound substructures using a FOF (Friends-of-Friends) and then the SUBFIND algorithm (Springel 2001) and tracked over time by the SUBLINK merger tree algorithm (Rodríguez-Gomez et al. 2015). Halo masses ( $M_{200}$ ) are defined as all matter within the radius  $R_{200}$  for which the enclosed mean density is 200 times the critical density of the Universe. In each FOF halo, the central galaxy (subhalo) is the first (most massive) subhalo of each FOF group. Its satellites are the remaining galaxies within the FOF halo. The stellar mass of a galaxy is defined as all the stellar matter assigned to host subhaloes.

### 2.1. Object selection

The suite of our zoom-in simulations is based on barred galaxies formed in the TNG50 simulation. For this, we use the bar catalogue of (Rosas-Guevara et al. 2022, herein RG22) and select central disc galaxies with a bar at  $z = 0$ . We select those whose dark matter haloes with masses ( $M_{200}$ ) between  $10^{11.5}$  and  $10^{12} M_\odot$  comparable to the Milky-Way like halo, yielding 31 galaxies. Furthermore, we concentrated on relatively isolated haloes. In particular, we used the tidal parameter that is defined as  $\tau = M_{200,i}/M_{200,tar}(R_{200,tar}/R_i)^3$  (Dahari 1984), where  $M_{200,i}$  and  $M_{200,tar}$  are the halo masses of the closest massive neighbour and the target halo, respectively.  $R_{200}$  is the size of the target haloes and  $R_i$  is the distance to the closest massive neighbour. We calculate  $\tau$  of our possible haloes candidates in order to assess the interaction strength between our candidates and their closest massive companion. This allows us to choose MW-like haloes that are isolated in the TNG50 dark matter simulation. We calculated the tidal parameter for our halo candidates and selected those with values lower than  $10^{-9}$ . This condition corresponds to those haloes whose closest massive neighbour galaxy is smaller than the candidate halo ( $M_{200,tar}$ ) and at a distance of  $10R_{200,tar}$  (see Grand et al. 2017). We also verify that these galaxies have relatively quiet merger histories (no more than two major mergers in  $z < 2$ ). We select six dark matter halos from the TNG50 simulations (Nelson, et al. 2019a) whose baryonic counterpart is a disc galaxy with a stellar mass  $> 10^{10} M_\odot$  and have a small bulge ( $B/T$  lie between 0.12 and 0.25). These galaxies hold a stable bar at  $z = 0$  that has formed between  $z = 1.5$  and  $z = 3$ . The bar sizes lie between 2 and 7 kpc, and most of the bars are strong bars ( $A_{2,max} > 0.3$ , see Appendix A for bar identification method). The right panel of Fig. 1 shows mock im-

ages (taken from TNG database Pillepich et al. 2019) in JWST NIRCам F200W, F115W, and F070W filters of the six barred galaxies from the TNG50 that were resimulated in this work and Table 1 shows some properties of the bars and discs. It is interesting to note that 5 of the 6 haloes belong to the catalogue of Milky Way analogues from TNG50 (Pillepich et al. 2023). The left panel of Fig. 1 depicts the dark matter density map of the TNG50 simulation, and the magenta circles mark the locations of the selected haloes which are not located in the densest regions of the cosmic web.

## 2.2. Initial Conditions

The initial conditions for the zoom-in simulation suite were created by selecting all dark matter particles in the TNG50 parent simulation at  $z = 0$  that are located within  $3 \times R_{200}$  (or  $5 \times R_{200}$  in cases where the former was not sufficient to get contamination free objects) of the centres of the chosen objects. The particles were then traced back to the starting redshift of the TNG50 simulation to obtain the Lagrangian region of each object. Next, a tree structure was used to produce the unperturbed particle distribution for each zoom-in simulation. Within the Lagrangian region, the tree was refined down to the same resolution as the initial particle distribution in the TNG50 simulation. Then layers of lower resolution boundary particles were added, with the resolution set based on the distance to the nearest edge of the high-resolution region, until a base resolution (corresponding to 135 particles on a side) was reached that covers the remaining part of the TNG50 volume. Perturbations were added at  $z = 127$ , the starting redshift adopted in the zoom-in simulations, using the Zeldovich approximation. Mode amplitudes and phases were drawn in Fourier space using the same random number seed and algorithm as in the *N-GENIC* code (Springel 2015), so that perturbations consistent with the TNG50 parent simulation were imprinted. For lower resolution boundary particles, only modes up to the Nyquist frequency that corresponds to that resolution level were included. An updated version of the employed zoom-in initial conditions code will be presented in Puchwein et al. (in prep.).

Upon starting the *AREPO* simulations, the particles in the initial conditions file are split into dark matter and gas components and then diagonally displaced with respect to each other by half a diagonal particle spacing, while keeping the centre of mass unchanged. A uniform magnetic seed field with a comoving field strength of  $10^{-14}$  Gauss is assumed at the initial redshift.

## 2.3. The galaxy formation model and their variations

We used the IllustrisTNG galaxy formation model (The Next Generation) project<sup>1</sup> (Nelson et al. 2018; Naiman et al. 2018; Pillepich et al., 2018b; Marinacci et al. 2018; Springel et al. 2018) and its predecessor *ILLUSTRIS* (Vogelsberger, et al. 2013; Vogelsberger et al. 2014a; Vogelsberger et al. 2014b; Genel et al. 2014; Nelson et al. 2015; Sijacki et al. 2015) with changes to star formation feedback, supermassive black hole growth, AGN feedback, and stellar evolution and chemical enrichment.

Gas radiative mechanisms are implemented with primordial (Katz et al. 1996) and metal line cooling, and heating by a time-dependent ultraviolet background field from stars and luminous AGN (Faucher-Giguère, et al. 2009). Star formation in the dense interstellar medium is treated stochastically following an empirical Kennicutt-Schmidt relation (Springel & Hernquist 2003).

<sup>1</sup> (Nelson, et al. 2019a); <http://www.tng-project.org>

Each stellar particle represents a population of stars with a common birth time following a Chabrier initial mass function. The stellar evolution is modelled in order to calculate chemical enrichment and mass expelled into the interstellar medium due to AGB stars, SNIa and SNII. Also, the evolution and production of ten elements (H, He, C, N, O, Ne, Mg, Si, Fe, & Eu) are individually tracked.

Previous studies have shown that physical processes that regulate star formation in galaxies can affect the formation of a bar (e.g. Bonoli et al. 2016; Zana et al. 2019; Irodotou et al. 2022). Taking advantage of this, combined with the parametric study done for the TNG collaboration Pillepich et al. (2019), we examine variations in physical processes that regulate the star formation of galaxies. We can divide these variations into two categories: (1) Those models that present modifications in the galactic winds generated for star formation, and (2) those models that present modifications in the BH physics of the model. The models of winds generated from star formation and AGN feedback will be explained in detail in the following subsections.

### 2.3.1. The galactic wind model and its variations

For our suite of the zoom-in simulations, we use the TNG model for galactic-scale, star formation-driven kinetic feedback (Pillepich et al., 2018b). In this model, wind particles absorb the thermal energy of the inherited gas cell and are injected isotropically. The initial orientation of the wind particles is random and are launched with an initial speed that scales with the local, one-dimensional dark matter velocity dispersion  $\sigma_{\text{DM}}$  (as in Eq. (14) of Oppenheimer & Davé 2006, 2008; Vogelsberger, et al. 2013), calculated with a weighted kernel over the  $N = 64$  nearest DM particles. In addition, the wind velocity has a dependency on redshift and a minimum value  $v_{w,\text{min}}$  given by

$$v_w = \max[k_w \sigma_{\text{DM}} (H_0/H(z))^{1/3}, v_{w,\text{min}}], \quad (4)$$

where  $k_w$  is a dimensionless parameter. Note that the wind velocity depends on redshift, this ensures that wind velocity and virial halo mass increase in scale with redshift in the same way (see Pillepich et al., 2018b). This choice of redshift-independent wind velocities at constant halo mass is motivated by semi-analytical model findings, where a comparable approach was required to recreate observed stellar mass functions and rest frame B- and K-band brightness functions throughout redshift (Henriques et al. 2013).

Once the wind injection velocity is known, the wind mass loading factor is determined by the specific energy available,  $e_w$ , which is connected to the energy released by SNII per produced stellar mass in the model. The TNG model includes two categories that affect the available wind energy: (i) some fraction of this energy is thermal, as determined by a parameter  $\tau_w$ ; and (ii) wind energy is dependent on the metallicity of the star-forming gas cells, such that galactic winds are weaker in higher metallicity environments. The mass loading factor upon injection is calculated as follows:

$$\eta_w = \dot{M}_w / \dot{M}_{\text{SFR}} = \frac{2}{v_w^2} e_w (1 - \tau_w), \quad (5)$$

where  $\dot{M}_w$  corresponds to the rate of gas mass to be converted into wind particles and  $\dot{M}_{\text{SFR}}$  the instantaneous, local, star formation rate. Then the wind energy available from the star-forming gas cells depends on metallicity  $Z$  as follows:

$$e_w = \bar{e}_w [f_{w,Z} + \frac{1 - f_{w,Z}}{1 + Z/(Z_{w,\text{ref}})^{\gamma_{w,Z}}}] N_{\text{SNII}} E_{\text{SNII},51} 10^{51} \text{erg} M_{\odot}^{-1}, \quad (6)$$

**Table 1.** TNG50 galaxy sample at  $z = 0$ . From left to right: Galaxy ID from TNG50 simulation, the logarithm of halo mass, disc (thin and thick components) to total mass fraction from kinematic decomposition (from fitting surface density stellar profiles as described in Appendix A, bulge (classical component) to total mass fraction from kinematic decomposition (from fitting surface density stellar profiles), the effective radius from the bulge calculated from a Sersic profile, the disc scale length (fitting face-on stellar surface density profiles of the kinematic component), bar strength and bar length (using Fourier decomposing face-on stellar surface density as described in Appendix A.1.

Galaxy ID	$\log_{10}(M_{\text{crit}200})$	$\log_{10}(M_*)$	$D/T ((D/T)_{\text{pso}})$	$B/T ((B/T)_{\text{pso}})$	$R_{\text{eff,bulge}}$	$h_{\text{disc}}$	$A_{2,\text{max}}$	$r_{\text{bar}}$
	$\log_{10}(M_{\odot})$	$\log_{10}(M_{\odot})$			kpc	kpc		kpc
560751	11.90	10.62	0.53 (0.69)	0.25 (0.29)	0.92	4.52	0.57	6.48
563732	11.91	10.56	0.58 (0.75)	0.26 (0.12)	0.81	5.51	0.55	2.64
569251	11.84	10.60	0.85 (0.84)	0.07 (0.11)	0.91	3.58	0.61	3.52
574286	11.71	10.34	0.68 (0.74)	0.11 (0.20)	0.42	2.56	0.53	2.40
547293	11.96	10.73	0.81 (0.71)	0.05 (0.24)	1.10	2.72	0.48	5.28
543376	11.97	10.79	0.67 (0.85)	0.12 (0.13)	0.90	5.78	0.38	2.16
<b>Median</b>	<b>11.91</b>	<b>10.61</b>	<b>0.67 (0.73)</b>	<b>0.12 (0.17)</b>	<b>0.91</b>	<b>4.05</b>	<b>0.54</b>	<b>3.08</b>

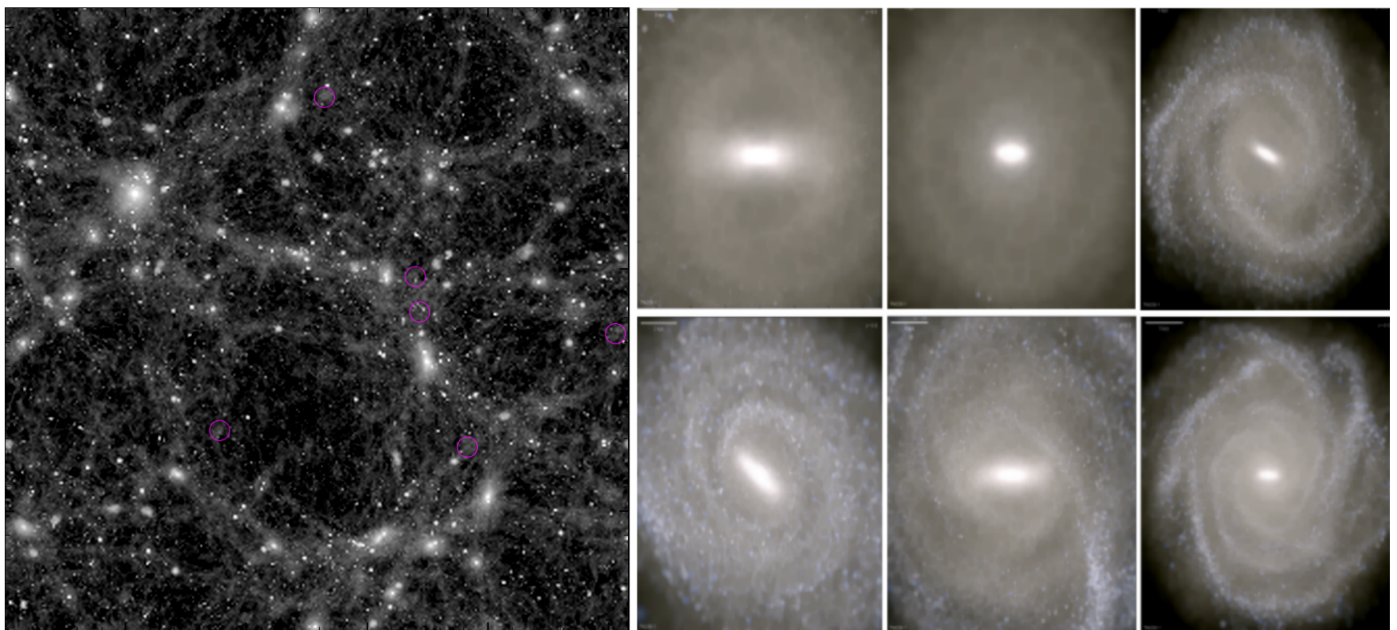


**Fig. 1.** Left panel: Dark matter distribution of the TNG50 simulation. Pink empty circles show the position of the selected haloes of the zoom-in simulations. Right panel: mocked images in JWST NIRCcam F200W, F115W, and F070W filters (face-on) calculated in Nelson et al. 2018, (TNG database) for the TNG50 galaxies that are resimulated. The NIRCcam blue channel highlights the young population of the galaxy, and the NIRCcam red channel older populations.

where  $\bar{e}_w$  is a dimensionless free parameter of the model,  $E_{\text{SNII},51}$  denotes the available energy per core-collapse supernovae in units of  $10^{51}$  erg.  $N_{\text{SNII}}$  is the number of SNII per formed stellar mass (in solar mass units) and depends on the shape of the IMF and the assumed minimum mass of core-collapse supernovae.  $f_{w,Z}$  is a parameter that reduces the energy at injection for gas cells with metallicities much larger than a given value  $Z_{w,\text{ref}}$ .

We focus on the energy available from star-forming cells of the galactic winds per time in our suite of zoom-in simulations, which limits the intensity of the galactic wind. The energy is regulated by the dimensionless free parameter,  $\bar{e}_w$ , which is between  $\bar{e}_w = 0$  and  $\bar{e}_w = 7.2$ . These values correspond to the No Wind (NW) model and the Strong Wind (SW) model, respectively. The value  $\bar{e}_w = 3.6$  is employed in the TNG50 simulation, and we refer to it here as the TNG50-like model (TNG50-like). In total, we have five modifications, including Weaker Winds (WW)

and medium Winds (MW). These variations are summarised in Table 2.

We remark that some of these variations have been explored to see their impact on the complete galaxy population in Pillepich et al., (2018b). We can see in their Fig. B1 how the global star formation history of a galaxy population can be affected by the strength of the winds. It is also worth mentioning that we have tried other variations at low resolution, such as a higher fraction of the thermal energy in the wind ( $\tau_w$ ) or higher wind velocity ( $\kappa_w$ ), and we found that the effects on the star formation of a galaxy were similar as varying  $\bar{e}_w$ . However, at high redshift, the variations in the strength of the winds  $\bar{e}_w$  affect the star formation density of the galaxy population (see Fig B1 of Pillepich et al., 2018b).

**Table 2.** Variations in the TNG galaxy formation model. We present the modified parameters in the galactic wind and quasar BH physics models. From left to right: Model name, wind strength parameter (Eq.6), and BH feedback efficiency in quasar mode (Eq. 10). In the case of No wind/ No black hole models, all the parameters related to the model were set to 0.

Name	$\overline{e_w}$	$\epsilon_{f,\text{high}}$
NW (no winds)	–	0.1
WW (weaker winds)	<b>1.8</b>	0.1
TNG50-like	<b>3.6</b>	0.1
MW (medium winds)	<b>5.4</b>	0.1
SW (strong winds)	<b>7.2</b>	0.1
NBH (no black holes)	3.6	–
BHlowEff	3.6	<b>0.05</b>

### 2.3.2. The BH model and its variations

The other model used in our suite of zoom-in simulations is the subgrid physics of supermassive black holes (BHs) that was presented in Weinberger et al. (2017). The BHs are formed in massive haloes ( $M > 7.38 \times 10^{10} M_\odot$ ) with an initial black hole mass of  $1.18 \times 10^6 M_\odot$ , and can grow via two growth channels: BH mergers and gas accretion. Gas accretion is Eddington-limited and allowed to accrete at the Bondi-Hoyle-Lyttleton accretion rate. To define high accretion and low accretion states, it is checked whether the Bondi-Hoyle-Lyttleton accretion rate exceeds a specific fraction of the Eddington limit by

$$\dot{M}_{\text{Bondi}} / \dot{M}_{\text{Edd}} \geq f_{\text{Edd,th}} \quad (7)$$

where the Bondi-Hoyle-Lyttleton accretion rate and the Eddington limit are defined respectively as

$$\dot{M}_{\text{Bondi}} = \frac{4\pi G^2 M_{\text{BH}}^2 \rho}{c_s^3} \quad \text{and} \quad \dot{M}_{\text{Edd}} = \frac{4\pi G M_{\text{BH}} m_p}{\epsilon_r \sigma_T c} \quad (8)$$

where  $c$  the speed of light in vacuum,  $m_p$  the mass of the proton, and  $\sigma_T$  the Thompson cross-section.  $\epsilon_r$  represents the radiative accretion efficiency.  $M_{\text{BH}}$  is the mass of the black hole, while  $\rho$  is the gas density of the surrounding gas;  $c_s$  is the effective speed of sound near the black hole and corresponds to  $(c_{s,\text{therm}}^2 + B^2/4\pi\rho)^{1/2}$ . The  $f_{\text{Edd,th}}$  scales with black hole mass to promote the transition from high to low accretion rates for the most massive black holes at late times, such that

$$f_{\text{Edd,th}} = \min \left[ f_{\text{Edd,0}} \left( \frac{M_{\text{BH}}}{10^8 M_\odot} \right)^\beta, 0.1 \right] \quad (9)$$

where  $\beta$  and  $f_{\text{Edd,0}}$  are both free parameters. It is worth noting that the values of  $f_{\text{Edd,0}}$ ,  $\beta$ , and the threshold mass  $10^8 M_\odot$  do not have independent values. These values were selected so that the most massive black holes can attain the low accretion rate state while the less massive ones struggle to do so.

In the model, there are two modes of AGN feedback, and the transition between the modes is given by Eq. 9. The two modes are (i) thermal *quasar mode* that heats the surrounding gas of the BH at high accretion rates (Springel et al. 2005; Di Matteo et al.

2005). The feedback energy in the *quasar mode* is released continuously as thermal energy that is injected into the surrounding gas given by

$$\Delta E_{\text{high}} = \epsilon_{f,\text{high}} \epsilon_r \dot{M} c^2 \Delta t \quad (10)$$

where  $\epsilon_r$  is the radiative efficiency, taking typical values between 0.04 – 0.4, for optically thin, geometrically thin, and radiatively efficient accretion discs depending on the SMBH spin. In the original TNG runs, it has been set to 0.2, and we do not change it to prevent additional degeneracy. The parameter  $\epsilon_{f,\text{high}}$  is the fraction of energy in *quasar mode* that couples with the surrounding gas, set to be 0.1 in the original TNG simulation. (ii) The second mode is the kinetic *wind mode* that produces winds, typically when the SMBH is massive enough and is subject to low accretion rates. For our suite of zoom-in simulations, we consider two variations in the quasar mode feedback: (1) the model **NBH**, which is a simulation performed without BH physics, and (2) **BHlowEff**, where the energy fraction that couples to the surrounding gas in the AGN feedback in quasar mode,  $\epsilon_{f,\text{high}}$ , is set to a lower value or 0.05. Both models are compared to the TNG50-like model, which takes the same parameters as the parent simulation TNG50. The values adopted for the modified parameters are found in Table 2.

### 2.4. Kinematic decomposition and identification of bars

To identify the different morphological components of each galaxy, we employ the kinematic decomposition algorithm MOR-DOR (Zana et al. 2022) to determine more specific galaxy components. The decomposition is based on the circularity ( $\epsilon$ ) and binding energy ( $E$ ) phase space, where a minimum in  $E$  is identified. The methodology identified five components: classical bulge, pseudobulge, thin disc, thick disc and stellar halo. To calculate the disc size, we use the face-on stellar surface density profiles of the total disc (thin and thick components), fitting an exponential profile. If a bar is present, we identify it using the Fourier decomposition of the face-on stellar surface profile and calculate the bar strength and length as in Rosas-Guevara et al. (2022). The thickness of the disc (using both thin and thick components) was calculated by fitting the edge-on surface density of the disc component with a square arc secant function in terms of the z-direction. In the case of the bulge size, we employ the face-on stellar surface density profiles, which are simultaneously fitted to the sum of a Sersic and an exponential profile for unbarred galaxies and the sum of two Sersic and an exponential profile where a bar is identified using the Fourier decomposition of the face-on stellar surface profile. Examples and more details of kinematic decomposition, identification of bars and the method of three-component decomposition of surface face-on density profiles can be found in Appendix A. Table 3 shows the median values of the bulge and disc structural properties for the different models. It also includes the median values of the bar strength and length for the models. We do not find any particular trend for the bar strength when we vary models since the relation of the bar length with stellar mass is flat, indicating no direct dependence on stellar mass. From hereafter, we refer to a disc as the sum of the thin and thick disc components and a bulge as a classical bulge.

## 3. Impact on bar and galaxy properties

In this section, we investigate the impact of altering the strength of the winds and BH physics on the properties of the galaxies and their structural parameters as a function of redshift.

**Table 3.** Median properties of galaxies for variations in the galaxy formation model at  $z = 0$ . The methodology used to calculate the properties of the discs, bars, and bulges is provided in Appendix A. From left to right: Variation Model, the logarithm of halo mass, disc (thin and thick components) to total mass fraction from kinematic decomposition (from fitting the total surface density stellar profiles), bulge (classical component) to total mass fraction from kinematic decomposition (from fitting surface density stellar profiles), the effective radius from the bulge calculated from a Sersic profile, disc scale length from kinematic decomposition<sup>2</sup>, disc thickness fitting the edge-on surface density with a square arc secant function in the  $z$ -direction, bar length and bar strength using Fourier decomposing face-on stellar surface density.

Sim Name	$\log_{10}(M_{\text{crit}200})$ $\log_{10}(M_{\odot})$	$\log_{10}(M_*)$ $\log_{10}(M_{\odot})$	$D/T$ ( $(D/T)_{\text{fit}}$ )	$B/T$ ( $(B/T)_{\text{fit}}$ )	$R_{\text{bulge}}$ kpc	$h_{\text{disc}}$ kpc	$h_{z,\text{disc}}$ kpc	$r_{\text{bar}}$ kpc	$A_{2,\text{max}}$
NW (no winds)	11.98	11.06	0.48 (0.45)	0.21 (0.55)	0.44	1.33			
WW (weaker winds)	11.91	10.70	0.51 (0.59)	0.23 (0.35)	0.33	3.01	1.58	2.35	0.62
TNG50-like	11.95	10.72	0.74 (0.70)	0.10 (0.18)	0.64	2.98	2.01	2.45	0.50
MW (medium winds)	11.94	10.53	0.74 (0.88)	0.08 (0.11)	1.03	5.19	1.71	–	–
SW (strong winds)	11.93	10.43	0.67 (0.86)	0.09 (0.10)	1.04	4.47	2.00	–	–
NBH (no black holes)	11.94	10.62	0.72 (0.74)	0.10 (0.20)	0.55	3.41	1.66	2.70	0.57
BHlowEff	11.92	10.58	0.63 (0.78)	0.12 (0.16)	0.79	4.28	1.80	2.95	0.53

<sup>2</sup> The disc-scale length of galaxies in the no wind model is calculated using the stellar half-mass radius of the disc and assuming an exponential profile. We use this alternative because fitting an exponential profile of the disc stellar surface density fails due to the high density presented in the centre of these discs.

### 3.1. Properties of bars and galaxies at $z = 0$

The median mass of the halo in the original TNG50 simulation is  $M_{\text{crit}200} = 10^{10.91}M_{\odot}$  (see Table 1) and the median of the zoom-in haloes for the different models ranges between  $M_{200} = 10^{10.92}M_{\odot}$  (BHlowEff model) and  $M_{200} = 10^{10.98}M_{\odot}$  (NW model) at  $z = 0$  which is at most a difference of 0.06 dex in halo mass. This is not the case for the rest of the properties when higher dispersion is found in varying supernovae feedback. Table 3 shows some of the median properties of the galaxies and their bars at  $z = 0$ . The median stellar mass ranges between  $M_* = 10^{10.43}M_{\odot}$  (SW model) and  $M_* = 10^{11.06}M_{\odot}$  (NW model) at  $z = 0$ . When this is compared to the stellar masses of the halos in the original TNG50 simulations ( $M_* = 10^{10.61}M_{\odot}$ ) or TNG50-like model ( $M_* = 10^{10.72}M_{\odot}$ ), the difference varies between 0.4 and 0.2 dex in stellar mass. The most massive galaxies are those without SN feedback (NW model), whereas the least massive galaxies are those in the SW model. This is expected since Supernovae processes are known to be physical processes that eject gas or prevent gas from forming stars and could influence the angular momentum of the gas in the galaxy. It is interesting to note that the morphology roughly remains the same as in the original TNG50 simulations at  $z = 0$  in the sense that galaxies have a high disc dominant component, although the stellar mass and sizes of the disc and the bulge are different in all the models (see Table 3). The galaxies with the lowest  $D/T = 0.48$  ( $(D/T)_{\text{fit}} = 0.51$ , using Fitting surface profiles) are those in the NW model, whereas the highest  $D/T = 0.74$  ( $(D/T)_{\text{fit}} = 0.88$ ) are those in the MW model. In the case of the bulges, the lowest  $B/T = 0.09$  ( $(B/T)_{\text{fit}} = 0.10$ ) is for the galaxies in the SW model, whereas the highest  $B/T$  is for the galaxies in the NW model. The compactness also changes. The most compact and massive bulges and thinner and massive discs are those in galaxies in the NW model ( $R_{\text{bulge}} = 0.48$  kpc,  $h_{\text{disc}} = 1.36$  kpc,  $h_z = 0.55$  kpc). Note, however, that the radius of the bulge is larger in galaxies in the weak wind model. The least compact bulge ( $R_{\text{bulge}} \approx 1$  kpc) is found in the galaxies in SW and MW models. Also, the galaxies in SW and MW models exhibit the most extended and thicker discs found in galaxies with  $h_{\text{disc}} = 4.47$  kpc,  $h_z = 2.00$  kpc and  $h_{\text{disc}} = 5.19$  kpc,  $h_z = 1.71$  kpc, respectively. Regarding the

galaxy properties in the models varying BH physics, the galaxy properties are pretty similar to those in the TNG50-like model. The parent TNG50 galaxies exhibit a bar, while in the zoom-in simulations, 83% of them present a bar at  $z = 0$  (5 of 6 galaxies) in the TNG50-like model. This galaxy, in particular, does not form a bar in any of the models including the weak wind model where the bar is present in the other galaxies. The median bar sizes lie between 2 kpc and 3 kpc, all of which are strong bars ( $A_{2,\text{max}} \geq 0.4$ ) as in the parent TNG50 simulations. The top panel of Fig.2 illustrates two galaxies at  $z = 0$  that are subject to the various variations in the wind model from NW (no wind model) to SW (strong wind model). The face-on (top panels) and edge-on (bottom panels) stellar density maps are represented in each column, with the energy injection per SN event intensifying from left to right. The disc-like morphology of the galaxy is generally independent of the model, as mentioned previously. The figure shows that the bar does not form in either the NW model or the SW model. The galaxy appears to be more concentrated in the no-wind model, while the galaxy appears to be less concentrated in the SW model. The two objects exhibit this behaviour. The bar forms in the TNG50-like model and the WW model. For the MW model, only one of the galaxies forms a bar. It is essential to acknowledge, however, that the stellar bar properties, including its length and strength, are different for different models.

The two objects are also depicted in the bottom panel of Fig.2 in two distinct variations in the BH physics: a model without BH physics (NBH) and a BH with less efficient quasar AGN feedback (BHlowEff) when the BH is accreting at higher rates compared to the TNG50-like model but with the same stellar feedback assumed as in the TNG50-like model. We observe that galaxy morphology is not significantly altered by the variations in the BH model, as opposed to the variations in the wind models. However, the final properties of the bar and the evolution of the BH itself will differ.

### 3.2. Galactic bar and galaxy evolution

We focus now on the evolution of the bar and galaxy properties. Fig. 3 illustrates the median redshift evolution of the bar proper-

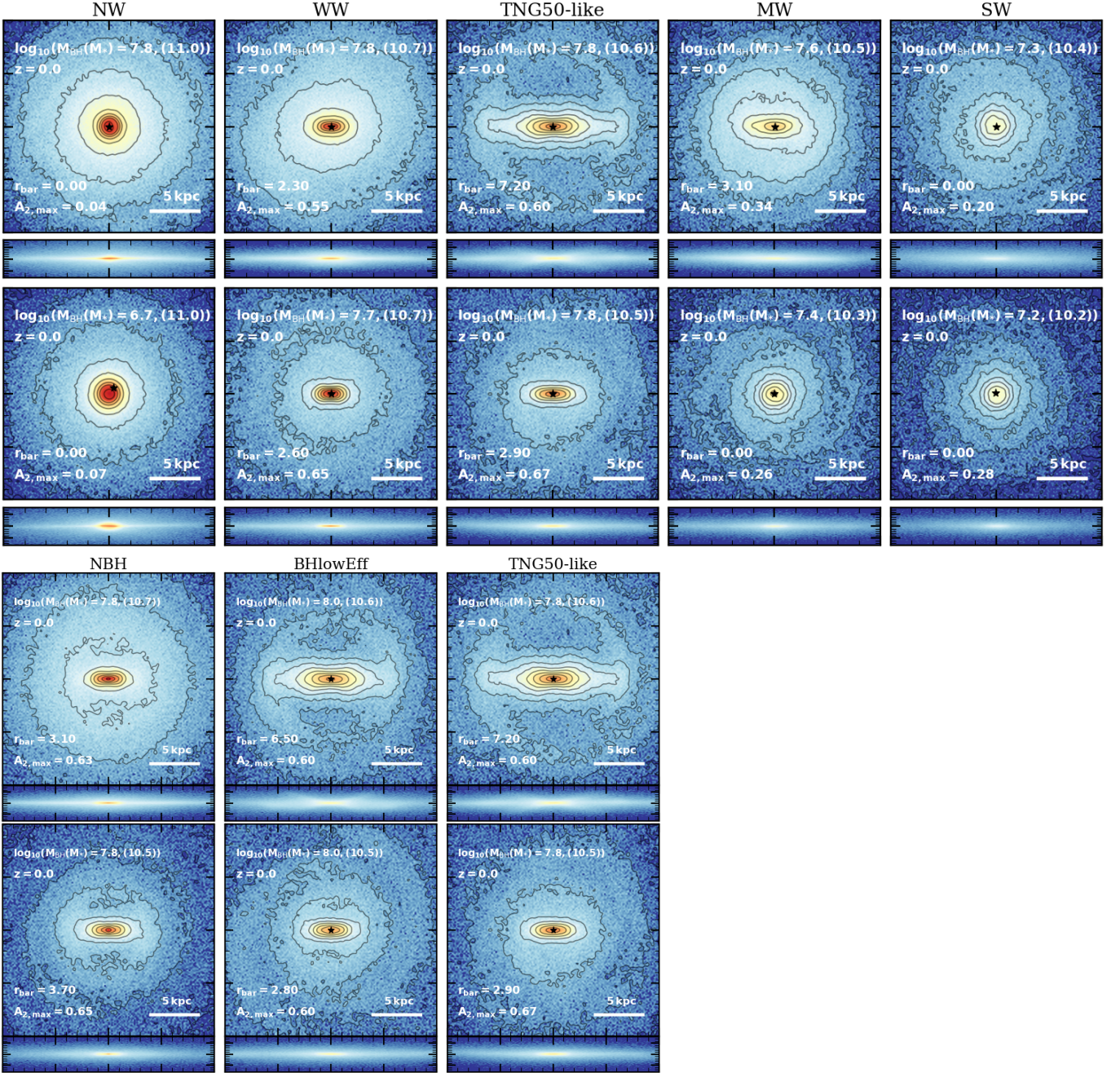


**Fig. 2.** Stellar density maps depicting the face-on view of two distinct galaxies at a redshift of  $z = 0$ . Top figure shows the wind model variations: each column corresponds to a distinct wind model, with the left column showing a galaxy without SN feedback and the right column galaxies with the strongest SN feedback. The bottom figure shows different quasar black hole models but with the same stellar feedback model as TNG50-like as indicated by Table 2. The black star symbolises the location of the black hole. It should be noted that in both the no wind and strong wind models, the disc galaxy does not exhibit the formation of a bar. Quasar black hole physics appears to have a limited influence on the formation of a bar.

ties and morphology of the galaxies for each of the four galactic winds models, the three BH models, and the galaxy counterparts in the TNG50 simulation. We observed that only the galaxies in the WW and TNG50-like models develop a stable bar in the galactic wind models. The galaxies in the other variations do not form a stable bar. We also observe that the weak wind model develops the strongest bars, which are also shorter in comparison to the galaxies in the TN50-like model. It is important to note, however, that galaxies in the no wind model develop non-axisymmetric instabilities, but they do not grow over time. This suggests that the disc may be unstable (see section 4); however, refrain from forming a bar. We observed that the galactic bar

formed earlier (see cyan vertical lines for the weak wind model,  $z_{\text{bf}} = 2.5$ ) compared to the TNG50-like models (black vertical lines, with  $z_{\text{bf}} = 2$ ). However, the scatter in the time of bar formation is large in all the models (see vertical colour lines in Fig. 3), including TNG50 galaxies. This could be attributed to the chaotic-like behaviour caused by feedback processes in the TNG model, affecting the scatter in some galaxy properties (Genel et al. 2019; Joshi et al 2024).

The morphology of the galaxies in the NW and WW models has been well-defined since early times. For instance, the galaxies in the no wind model have already assembled a substantial disc by  $z_{\text{disc}} = 3$  and also are the most massive galaxies in com-



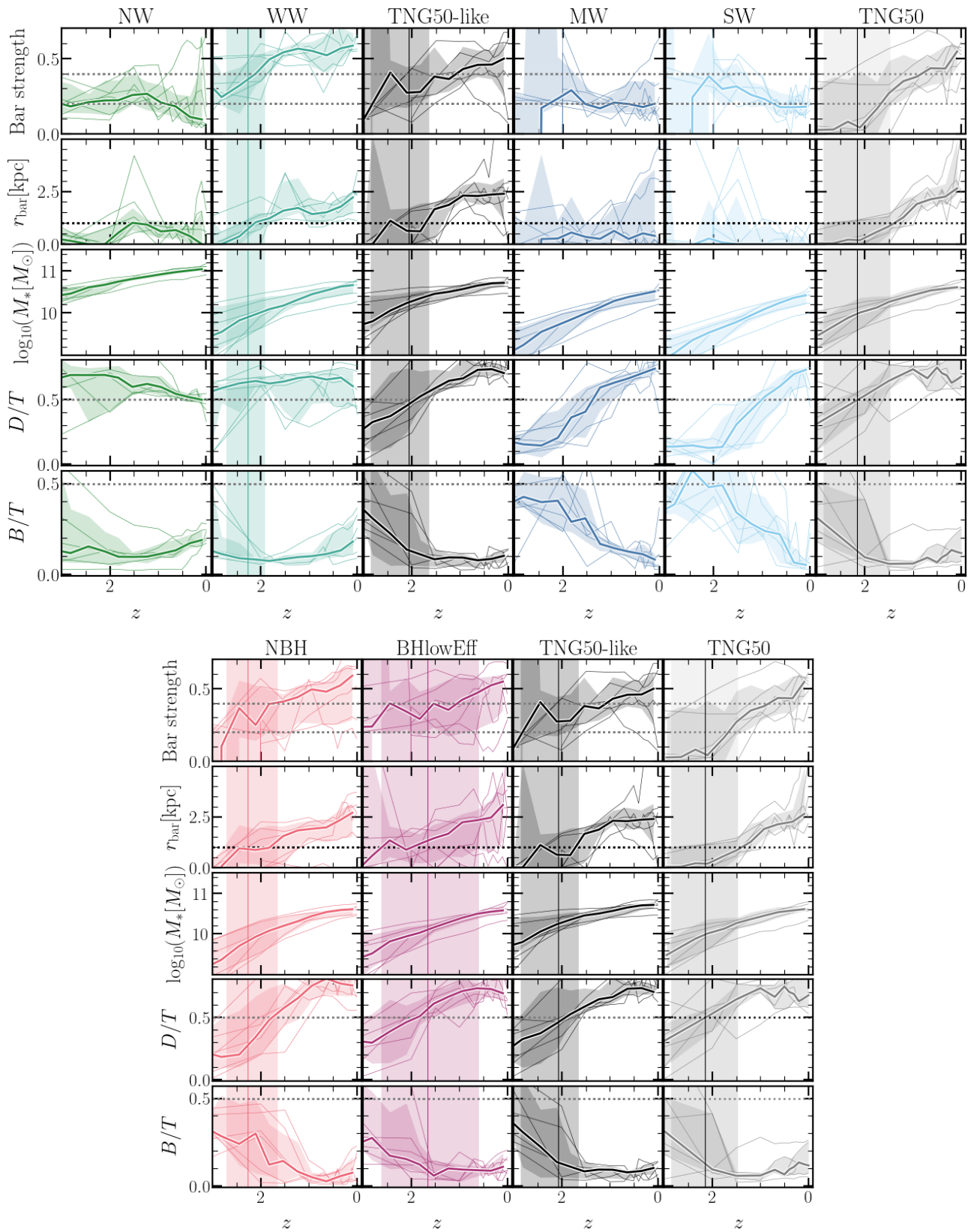


**Fig. 3.** The median evolution of the bar and galaxy morphology for simulations with different galactic wind (top set of panels) and black hole feedback (bottom set of panels) models. Each column corresponds to different models, as indicated in the figures. From top to bottom rows: the bar strength, bar extent, the stellar mass and the disc-to-total and bulge-to-total mass fraction are shown. The medians and the distribution between 20<sup>th</sup> and 80<sup>th</sup> percentiles correspond to solid lines and shaded regions, respectively. Thinner lines correspond to the evolution of each halo. Vertical solid lines and shaded region represent the median redshift and the distribution between 20<sup>th</sup> and 80<sup>th</sup> percentiles of the bar formation time. The stronger the wind, the lower the probability of the galaxy developing a bar, except for the no wind galaxy. The build-up of a well-defined massive cold disc is delayed for stronger galactic wind models. No significant change is seen in the black hole variation models.

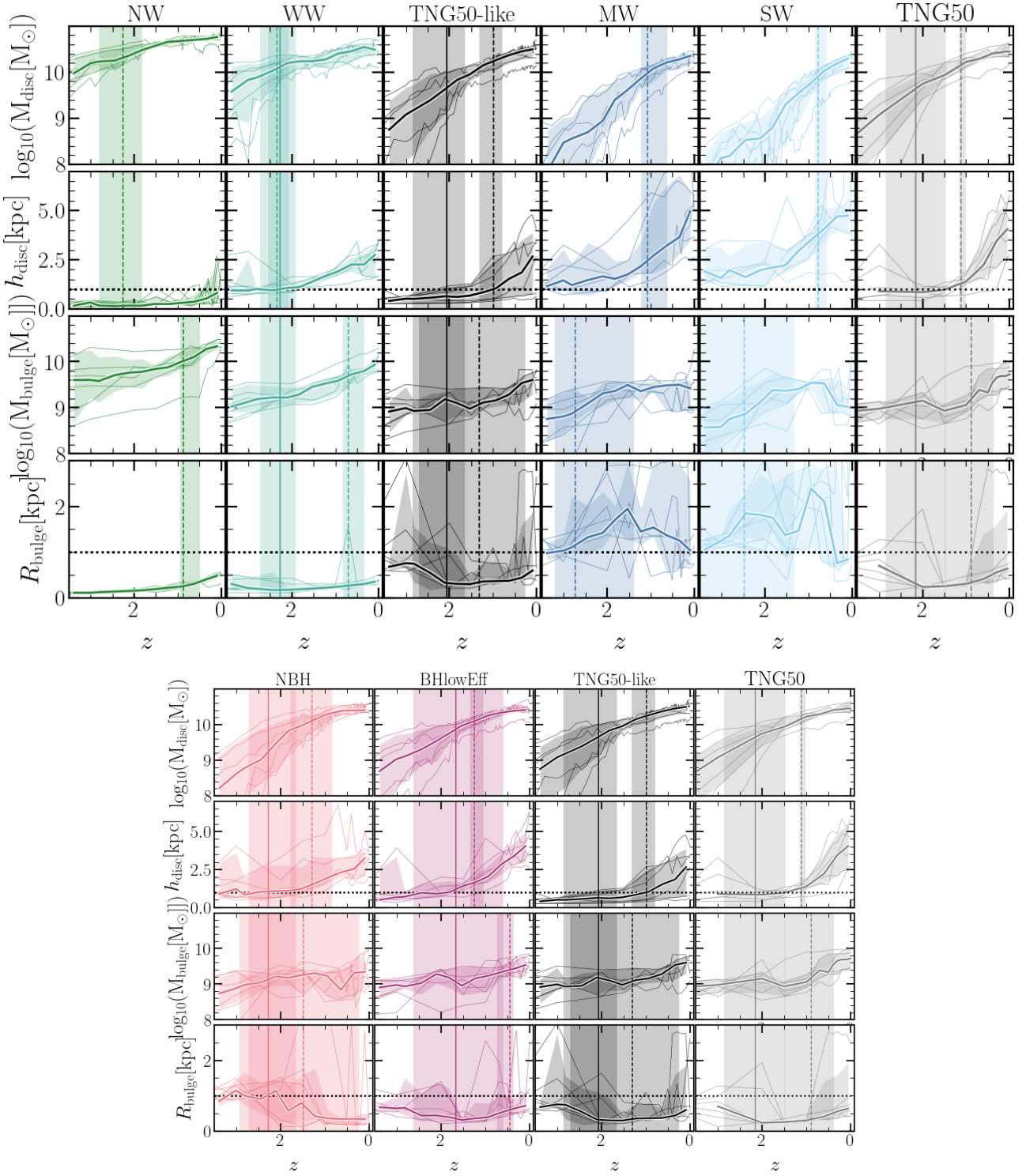


**Fig. 4.** The evolution of the disc (thin and thick components) and bulge masses and their sizes. From left to right columns: variations in the galactic winds models (top) and quasar BH physics models (bottom). The last column is the original TNG50. The medians and the distribution between 20<sup>th</sup> and 80<sup>th</sup> percentiles correspond to solid lines and shaded regions. Thinner lines correspond to the evolution of each halo. Vertical solid lines represent the median redshift of bar formation. Dashed vertical lines in the top rows panels correspond to the median redshift when the disc has assembled 50 per cent of its final mass, whereas the vertical dashed lines in the two rows panels correspond to the median redshift when the bulge has 50 per cent of its final mass. Vertical shaded regions represent the distribution between 20<sup>th</sup> and 80<sup>th</sup> percentiles.

parison to the other models. When we move to later times, the massive disc component is delayed when the wind intensity generated by SN feedback is greater, whereas the bulge forms earlier and is less massive in comparison to the disc. It should be noted that the bar formation seems to be linked to the earlier build-

up of the massive disc (see Zana et al. 2019; Rosas-Guevara et al. 2020; Izquierdo-Villalba et al. 2022). However, galaxies do not form a stable bar in the no wind model. Conversely, galaxies in the strong wind models developed a substantial disc that was later formed, but it never developed a stable bar. In the BH

variations models, the bar is present in all simulations, but the bar formation time varies dramatically. Additionally, we can observe some variations in the length and strength of the bars for galaxies across the various models. The BHLowEff variation, in particular, displays the bars with the highest length and strength.

Fig. 4 illustrates the evolution of the disc and bulge masses and their sizes in the galactic wind and the quasar BH physics models. The galaxies in all models possess a massive disc which is larger than  $10^{10}M_{\odot}$  and becomes dominant, but their build-up is distinct: the disc build-up is slower as the winds from supernova feedback become stronger. In order to quantify this, we calculate the formation time (redshift) of the massive disc by determining the time at which it reaches 50% of its  $z = 0$  mass. This is depicted as vertical dotted lines in the figures, with the 20th and 80th percentiles for all objects. These measured times (redshifts),  $t_{50,\text{disc}}(z_{50,\text{disc}})$ , show that the disc formation occurs later for galaxies in the strong wind model ( $z_{50,\text{disc}} = 0.8$ ) and earlier for galaxies in the no wind model ( $z_{50,\text{disc}} = 2.25$ ). Note that the scatter of  $z_{50,\text{disc}}$  in the variations of the BH model is higher than that in the TN50-like model, oscillating between  $z = 0.8$  and  $z = 1.3$  in the case of galaxies in the no black holes model. However, the growth of the disc is not significantly affected.

The second row of Fig. 4 illustrates the disc length. This generally increases with increasing time for all the models; however, the final disc length increases as the intensity of the galactic winds increases. The most extended and least dense discs are those in the strong wind model, while the most compact and dense are in the no wind model. This is important because these properties play a role in the bar formation criterion, as we will see in the next section.

The bulge growth for variations in the wind and BH models is illustrated in the third row of Fig. 4. The figures demonstrate that the bulge evolution is more intricate, particularly in light of the wind model variations. Additionally, it is important to observe that the fluctuations between galaxies in each model are greater. In contrast to the disc assembly, there are primarily two distinct behaviours. In some cases, the bulge forms later in time than the disc and the galaxy develops a bar, not necessarily a stable bar, as in the NW model ( $z_{50,\text{bulge}} < 1$ ). This phenomenon is observed in NW, WW, and TNG50 models, suggesting that the bar may facilitate the expansion of the bulge in these models after it has been established. The SN feedback intensity is high in models with moderate (MW) and (SW) strong winds, resulting in a more complex bulge build-up that is subject to significant fluctuations. Initially, the bulge experiences an increase in mass as time progresses, reaching up to 50% of its current mass even earlier. Subsequently, the bulge mass decreases over time. We track the stellar particles that are part of the bulge at the moment of their mass peak. We find that a fraction of the stellar particles that were not part of the bulge later in time present higher velocities and at larger distances, associated with the halo component. This might be due to a fast ejection of matter.

The bulge size is presented in the bottom panels of the figure. As the bulge mass, their evolution is more complicated, and it is more affected by the wind model variations. The bulge size increases with time for NW, WW, and TNG50-like models; the MW and SW models are more complicated and show similar fluctuations, as seen in the bulge mass attributed to the intensity of SN feedback. The most compact and massive bulges are those in the no wind model. The most extended and least massive bulges are found in the strong wind models.

In the strongly barred galaxies, discs and bulges are formed at a more rapid pace than those in unbarred galaxies. Our results suggest that gas is swiftly consumed to form stars in galaxies in

the models with NW, WW, and TNG50-like models, resulting in more dense discs and bulges. In contrast, galaxies in models with medium and strong feedback discharge gas at earlier times as a result of the less intense gravitational potential of the halo and the intense SN feedback. This would have an impact on the properties of the gas and the formation of stars from early times. This is in agreement with the result from Bi, Shlosman, & Romano-Díaz (2022a). The authors, using zoom-in simulations with a mass resolution compatible with the TNG50 simulation, find that SN feedback impacts the cold accretion flow (see their Figure 1) in high-redshift Milky-Way galaxies.

## 4. Bar formation

The primary results are detailed in this section. The structural parameters of a galaxy have been influenced by galactic winds since the earliest times, as demonstrated in previous sections. We observe the bar instability criteria in detail in various models, as they are contingent upon the structural parameters. In particular, we will be focussing on three criteria: the Toomre 1964 (Eq.1), Efstathiou, Lake & Negroponte 1982, (ELN) (Eq.2), and Mo, Mao, & White 1998, (MMW) (Eq. 3) criteria.

The evolution  $\epsilon_{\text{ELN}}$ ,  $\lambda_{\text{MMW}}$  and  $Q_T$  for the different models, is illustrated in Fig. 5. Except for galaxies in the no wind model, most of the galaxies in the models satisfied the ELN and MMW criteria for an unstable disc. In particular, for WW and TNG50-like models, both criteria have been satisfied since the time of bar formation, which is shown as the magenta-shaded region below the horizontal dotted line in the figure. In the case of the Toomre criterion, the values are more unstable. However, the galaxies in all the models roughly satisfy the Toomre criterion, except for galaxies in the no wind and weak wind models.

### 4.1. ELN criterion

In this section, we focus on the evolution of the disc mass and size evolution and the maximum circular velocity ( $V_{\text{max}}$ ) of the dark matter halo that concerns the ELN criterion Efstathiou, Lake & Negroponte 1982, (ELN). In the last section, in Fig. 4, we have studied the mass and size growth of the disc for the different galactic wind and BH model variations. We observe that the evolution of the disc scale length and the disc mass have been affected by the strength of the galactic winds (kinetic energy released into the ISM) since early times. The most extreme case is the variation where there is no galactic wind or, opposite, the galaxy experiences a strong galactic wind. In both NW and SW models, the galaxy forms a massive disc ( $M_* > 10^{10}M_{\odot}$ ) and a relatively small bulge ( $B/T < 0.4$ , see Table 3), and neither of both models forms a stable bar. The other models show an intermediate effect between these two examples, and only the galaxies in the TNG50-like and weak wind models form a bar. In contrast, the evolution of the maximum circular velocity ( $V_{\text{max}}$ ) of the dark matter halo almost remains constant across all scenarios, as seen in Fig. 6. There is no distinction when the dark matter halos are the sole factor considered. Therefore, the size of the disc is a determinant of the ELN criterion and, with less significance, the stellar mass disc. The ELN criterion fails to predict the disc stability of the galaxies in the no wind model while the ELN criterion is met by the galaxy in the WW and TNG50-like models, at least during the time of bar formation. In the case of the BH physics variations, there are some variations in the evolution of the disc size, but not in the disc mass. However, the values and evolution of the  $\epsilon_{\text{ELN}}$  parameter remain consistent, as seen in Fig. 5. The ELN criterion emphasises that a compact, dense disc

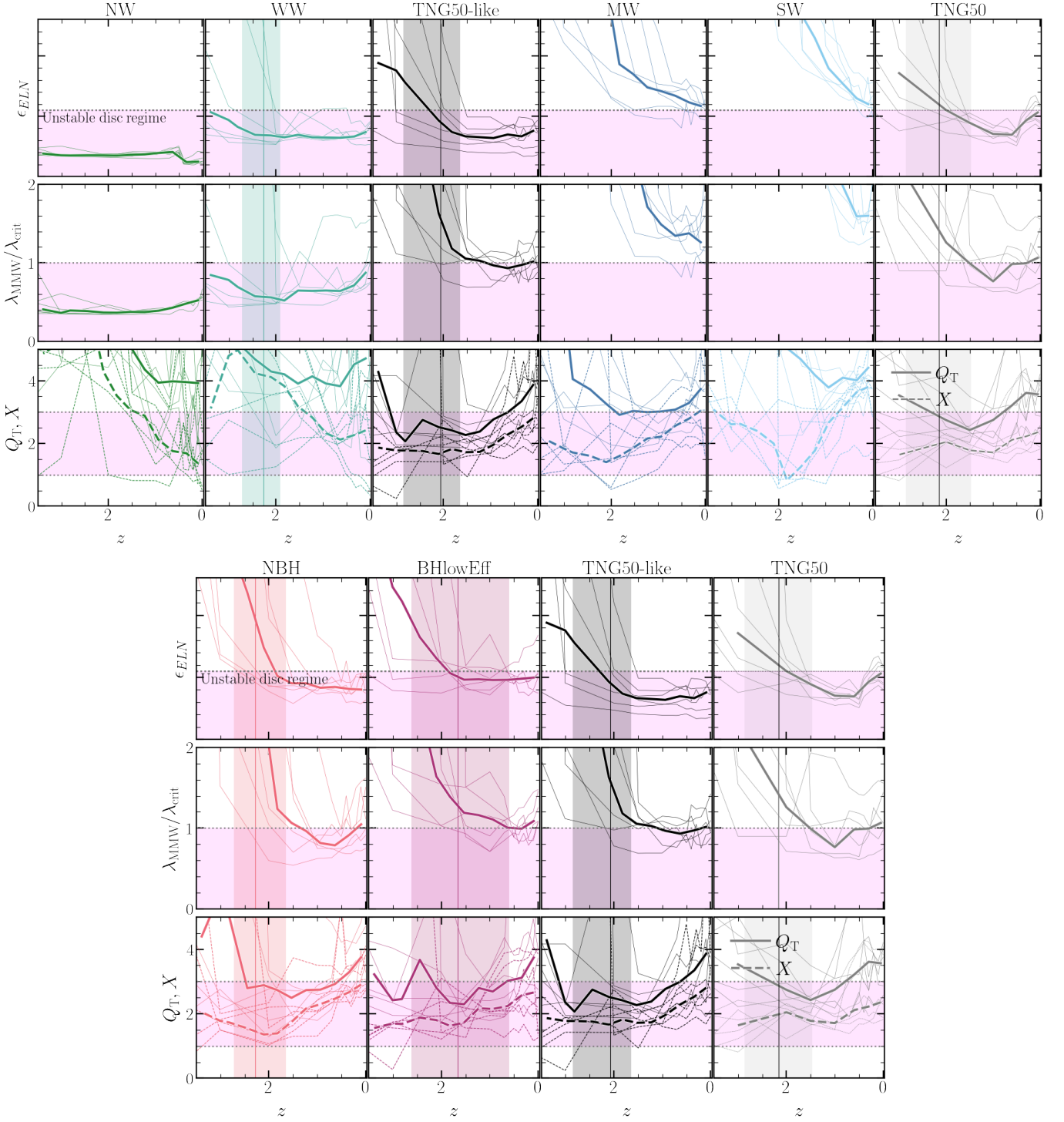


**Fig. 5.** From top to bottom: The evolution of the parameters relevant for bar formation. Shown are the ELN criterion (Eq.2), the MMW criterion (Eq.3) and the Toomre parameter (Eq. 1), for the different galactic wind models (top figure) and BH physics models (bottom figure) and the original TNG50. Horizontal dashed lines represent the threshold that defines if a disc is unstable and magenta shaded region represents the values where the disc is unstable. Thinner lines correspond to the evolution of each halo. Vertical solid lines and shaded region represent the median redshift and the distribution between 20<sup>th</sup> and 80<sup>th</sup> percentiles of the bar formation time.

is a prerequisite for forming a bar; however, our findings show this condition alone is not sufficient.

#### 4.2. MMW criterion

In order to conduct a more thorough investigation of the MMW criterion (Mo, Mao, & White 1998), the middle panels of Fig. 5

show the values of the parameter  $\lambda_{\text{MMW}}$ , and the magenta shaded region corresponds to the values of  $\lambda_{\text{crit}}$  as seen in Eq. 3. For details in the calculation of  $\lambda_{\text{crit}}$ , see Eqs. 23, 32, 34 in Mo, Mao, & White (1998). Therefore if  $(\lambda_{\text{MMW}}/\lambda_{\text{crit}}) > 1$ , the disc is approximately stable. For the galaxies in the models that form a bar,

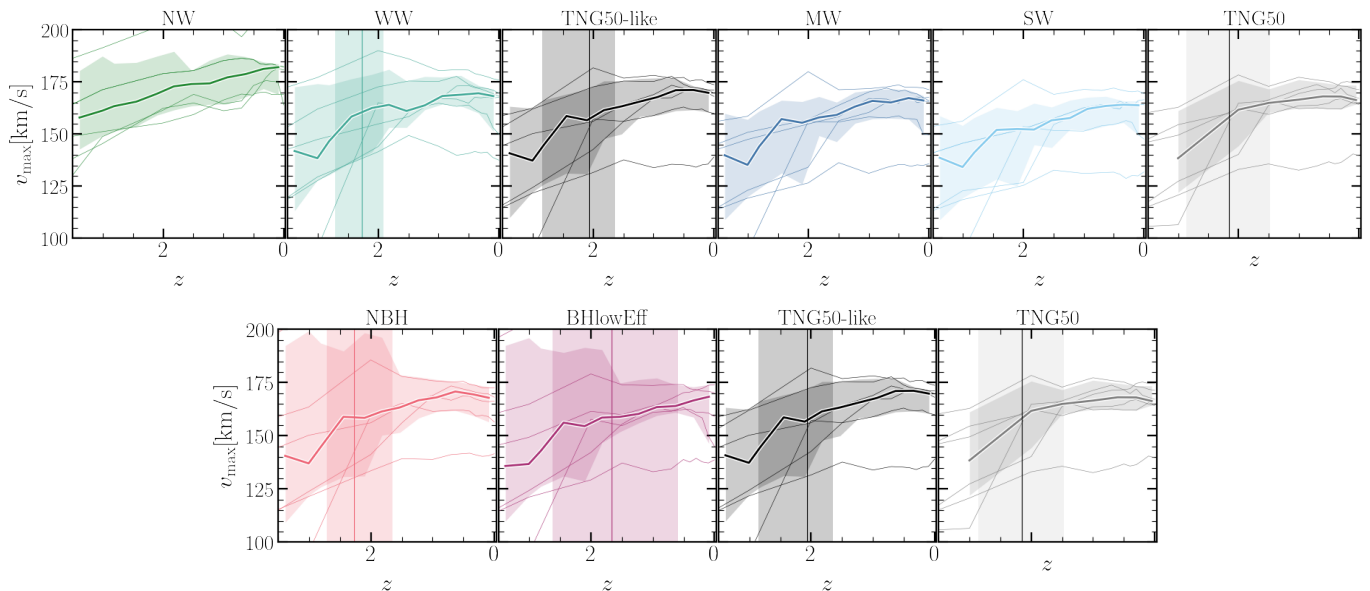


**Fig. 6.** The median evolution of the maximum velocity of the Dark Matter halo. The column represents the variations of galactic winds (upper figure) and BH physics models (bottom panels) in order of left to right, and vertical solid lines represent the bar formation redshift. The original galaxy in TNG50 is represented by the final right column. Thinner lines correspond to the evolution of each halo. Vertical solid lines and shaded region represent the median redshift and the distribution between 20<sup>th</sup> and 80<sup>th</sup> percentiles of the bar formation time.

the MMW criterion is satisfied. The values of  $(\lambda_{\text{MMW}}/\lambda_{\text{crit}}) \lesssim 1^2$  lies in the magenta-shaded region, suggesting that the galaxies are marginally or completely unstable, especially at the time of bar formation. An exception is the galaxies in the models without SN feedback, where the MMW criterion fails to predict that the disc is stable since a bar does not form. On the other hand, The MMW criterion is satisfied for galaxies in the models with medium and strong winds. For these models,  $(\lambda_{\text{MMW}}/\lambda_{\text{crit}}) > 1$  are above the shaded regions, indicating that the discs are stable.

The spin parameter, the ratio of the angular momentum of the disc and the halo and the ratio of the disc stellar mass and the halo mass are all presented in Fig. 7. The spin parameter evolution remains almost constant regardless of the galactic winds model or the varied BH physics with values between 0.02 and 0.04, with the exception of the no wind model, which exhibits values smaller than 0.03. This suggests that the spin parameter is almost not affected by SN feedback. The ratio between the angular momentum of the disc and that of the dark matter halo is subject to change as the intensity of the galactic winds is modified. This ratio increases over time, transitioning from values less than 0.02 at  $z = 2$  to values just smaller than 0.05 at  $z = 0$ , with the exception of the galaxies in the no wind model. These galaxies present high ratios and reach the highest value ( $J_{\text{disc}}/J_{\text{h}} \sim 0.06$  at  $z = 0$ ). The galaxies with the lowest values are those in the medium and strong wind models, nearly reaching 0.04 at  $z = 0$ .

Another property that is most significantly impacted in all the simulations is the ratio of disc mass to dark matter mass, which is a result of the regulation of star formation, as discussed for the  $z = 0$  properties in section 3. The ratio  $M_{\text{disc}}/M_{\text{h}}$  is significantly influenced by supernova feedback variations, with the highest values presented for the no wind model ( $\gtrsim 0.05$ ) and the lowest values for the strong wind models ( $\lesssim 0.02$ ). Apart from the no wind model, this ratio increases with time. The disc stability can

be approximated to a first degree if  $\lambda_{\text{MMW}} > (M_{\text{disc}}/M_{\text{h}})$  as  $\lambda_{\text{crit}}$  is not significantly influenced by the disc and halo models. This condition is indeed satisfied for unbarred galaxies in the medium wind and strong wind models, as we have observed. On the other hand, for weaker wind and TNG50-like models, the barred galaxies have marginally unstable discs at the time of bar formation according to the MMW criterion. Galaxies in the no wind model also present an unstable disc, although a stable bar does not form. Besides, these galaxies exhibit  $J_{\text{disc}}/J_{\text{h}} < (M_{\text{disc}}/M_{\text{h}})$  and produce galaxies that are very compact, which exemplifies the necessity of SN feedback to regulate star formation at early times to shape the formation of discs as observed in the local Universe (Navarro & Benz 1991).

#### 4.3. Toomre Criterion and Swing parameter

As discussed in the introduction, the (Toomre 1964,  $Q_{\text{T}}$ , see eq.1) is one of the criteria for bar instability. This parameter is responsible for disc stability in axisymmetric density perturbations. If  $Q_{\text{T}} < 1$ , the disc is unstable. In conjunction with the Toomre parameter, the swing parameter ( $X$ ) evaluates the amplification of the density perturbations through the swing amplification effect. It is defined by  $X = r\kappa^2/(4\pi G)\Sigma$ , where  $\kappa$  is the epicyclic frequency,  $G$  is the gravitational constant, and  $\Sigma$  is the stellar surface density. Both parameters  $Q_{\text{T}}$  and  $X$  depend on the disc kinematic properties as a function of radius. The Toomre parameter should be approximately 1, but it should be at most 2 to achieve substantial amplification (Binney & Tremaine 2008). To the extent that  $Q_{\text{T}}$  is excessively high, the disc is too stable to generate large-scale perturbations. In addition, a value in the range  $1 \leq X \leq 3$  suggests a regime in which swing amplification can substantially amplify non-axisymmetric perturbations, such as spirals or bars.

The bottom panels of Fig. 5 display the average  $Q_{\text{T}}$  and  $X$  for the various models within a stellar half-mass radius and a  $z$ -slide of 2 kpc, which is comparable to the thickness of a disc (refer to Table 3). We can observe that the values of  $Q_{\text{T}}$  and  $X$  are

<sup>2</sup> We used the assumption that the halo concentration  $c_{\text{NFW}} = 10$  in order to compute  $\lambda_{\text{crit}}$ ; however, we experimented with smaller/larger values and got comparable results. This is because the criterion weakly depends on concentration as seen in (Mo, Mao, & White 1998).

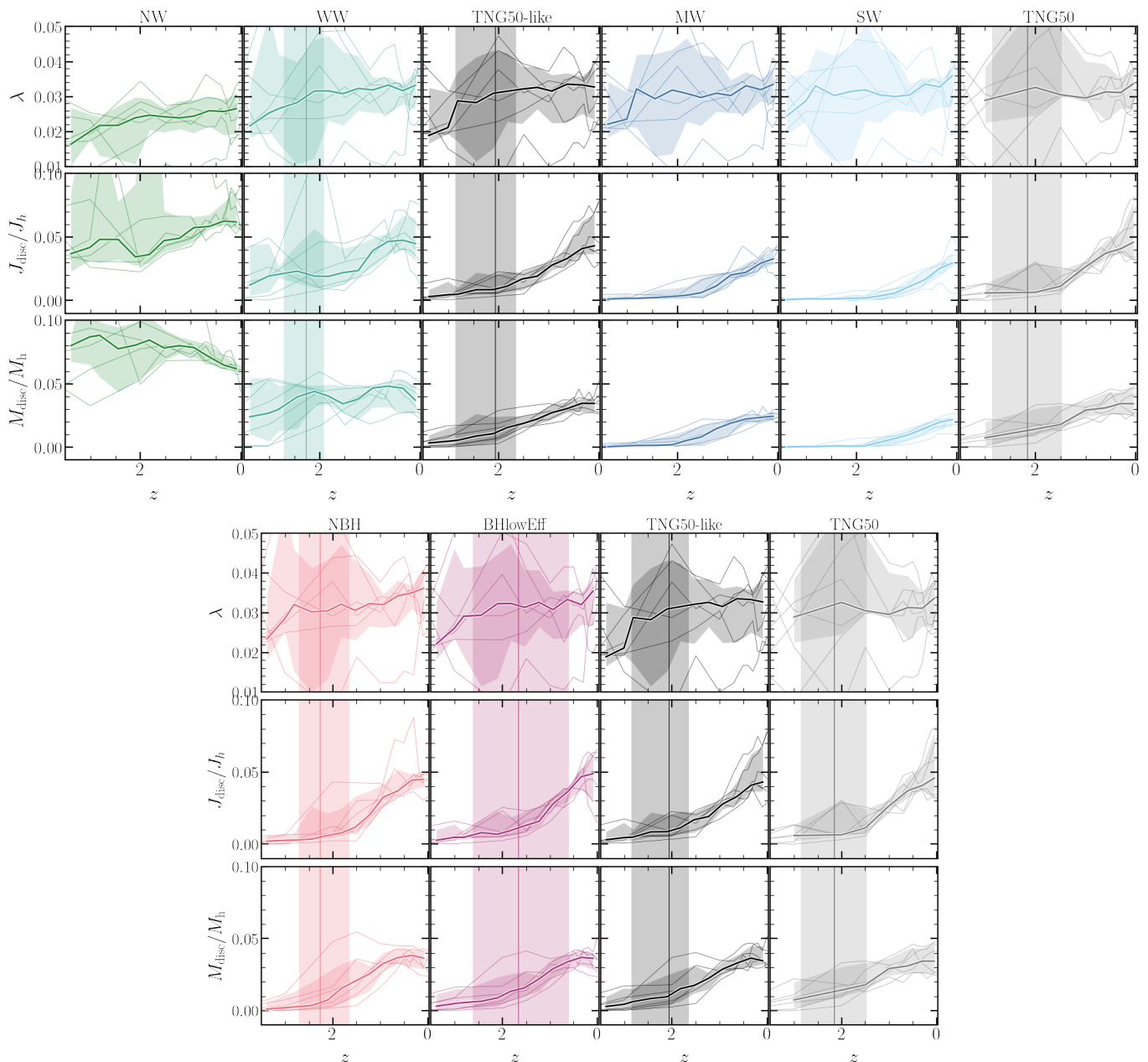


**Fig. 7.** From top to bottom: The median evolution of spin parameter, the ratio of the angular momentum of the disc over the halo and the disc mass fraction (solid thicker lines). From left to right column, different galactic wind models (top figure) and BH physics models (bottom figure) are shown. The rightmost column corresponds to the original galaxy in TNG50. Thinner solid lines correspond to individual halos. Vertical solid lines and shaded region represent the median redshift and the distribution between 20<sup>th</sup> and 80<sup>th</sup> percentiles of the bar formation time.

located in the bar instability region in the TNG50-like and BH variation models, particularly during the bar formation phase. It is interesting to note that the values of  $Q_T$  are just above 2 at later times. This is in agreement with the values presented in recent observations, which show that some observed barred discs can reach values of  $Q_T$  of  $\approx 3$  (Romeo, Agertz, & Renaud 2023). The swing parameter,  $X$ , is located in the instability regions of galaxies for all the models, especially in the medium and strong wind models, while  $Q_T$  is located above the instability region with values larger than 3 in both the medium and strong wind models. The high values of  $Q_T$  predict that the disc being highly stable against bar instabilities. Interestingly, the Toomre parameter is substantially higher in the no/weak wind model for galaxies ( $Q_T > 4$ ) than in the other models. We will focus on Fig.

8 to better understand this behaviour. We note that the galaxies in the no/weak wind models have higher  $\kappa$  values. However, they also have higher stellar surface densities, which could be used to offset the highest values in  $\kappa$ . Consequently, we obtained similar values in  $X$  at  $z \lesssim 2$ . However, the radial velocity dispersion, which is significantly influenced by the SN feedback, is the primary cause of the discrepancy in  $Q_T$  between the no/weak wind models and the other models. Also, this could be the reason for the opposite predictions between this instability criterion and the ELN and MMW criteria. The ELN and MMW criteria do not consider  $\sigma_R$  (Eqs. 2 & 3) while  $Q_T$  does depend on it (Eq.1). This will be discussed in the next section.

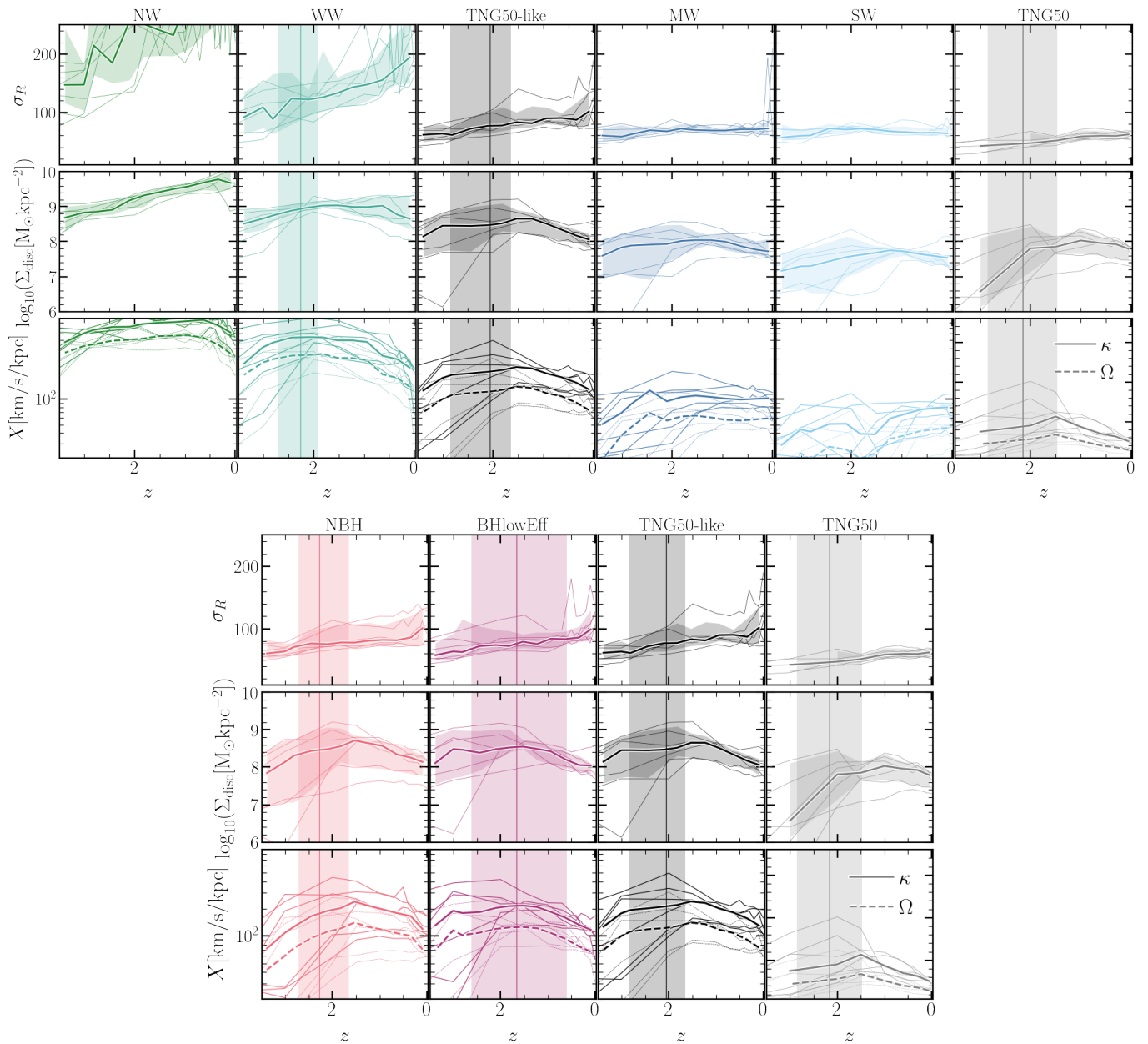


**Fig. 8.** From top to bottom: The evolution of radial velocity dispersion, stellar surface density, epicyclic and angular frequency in a stellar half-mass radius aperture. From the left to the right column, different galactic wind models (top figure) and BH physics models (bottom figure) are shown. The last right column corresponds to the original galaxy in TNG50. Thinner solid lines correspond to individual halos. Vertical solid lines and shaded region represent the median redshift and the distribution between 20<sup>th</sup> and 80<sup>th</sup> percentiles of the bar formation time. These three properties of the galaxy used in the Toomre parameter and Swing parameter are highly affected by the SN feedback process.

## 5. Discussion

In this section, we will discuss our findings with respect to previous works and future prospects.

### 5.1. Is bar formation affected by the central bulge?

The ELN and MWW criteria predict that the disc is unstable to bar-like perturbations for galaxies the no wind model; however, a stable bar does not form. These galaxies exhibit the highest stellar mass content in the disc since early times. For example, the findings of [Bonoli et al. \(2016\)](#) and [Spinoso et al. \(2017\)](#), which analyse the twin zoom-in simulations of the Milky Way, ErisBH and Eris, suggest that ErisBH forms a bar as a result of AGN

feedback, which diminishes the bulge size in comparison to Eris. This enables the activation of bar instabilities. In addition, [Saha & Elmegreen \(2018\)](#) demonstrate that cold stellar discs surrounded by an initial relative dense bulge ( $\rho_{\text{bulge}}/\rho_{\text{disc}} > 1$  for compact bulges) do not form a bar even though the disc was susceptible to bar instabilities (lower values of the Toomre parameter). Similarly, [Kataria & Das \(2018\)](#) found that massive and more concentrated bulges can inhibit bar formation and growth, particularly when the bulge-to-disc mass fraction is higher than 0.3 for concentrated bulges and even higher (0.6) for less concentrated bulges. This was achieved using N-body simulations.

Fig. 9 illustrates the bulge-to-total-mass fraction ( $B/D$ ) as a function of bulge-to-disc sizes ratio and colour-coded by redshift. Galaxies in the no wind model show an increase of  $B/D$

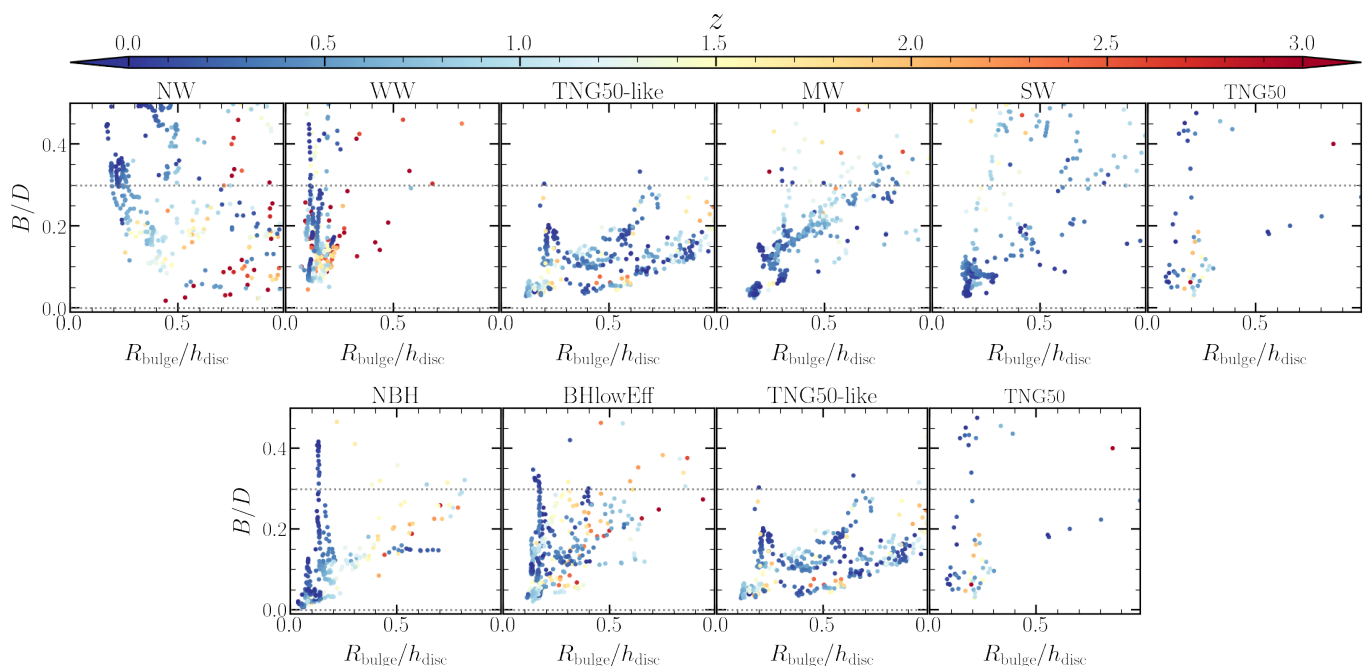


**Fig. 9.** The bulge-to-disc mass fraction as a function of bulge-to-disc size ratio. Columns from left to right: the galactic wind models (top figure) and BH physics model variations (bottom figure). Colour code represents the redshift. Horizontal grey dashed lines represent the limit given by Kataria & Das (2018) for dense bulges that do not favour the formation of a bar, even if the disc could be unstable.

with values higher than 0.3 and bulge-to-disc size ratios smaller than 0.5 after  $z = 1$ . The upper limit suggested by Kataria & Das (2018) for compact bulges to prevent bar formation is  $B/D = 0.3$ . Their simulations indicate that bars can only form in disc galaxies when the radial force due to the bulge is less than 0.35 in comparison to the total force at the disc scale length. This is an outcome of the bulge’s increasing mass, which increases the velocity dispersion of the disc and the radial force. At high redshift ( $> 1.5$ ), the galaxies in the no wind model, generally exhibit  $B/D < 0.3$ ; however, the bulge-to-disc size ratios take values higher than 0.5 (less compact bulges). Consequently, the disc is unstable in principle, but the non-axisymmetric instabilities are unable to grow (see Fig.3) since the bulge mass continues to increase (see Fig. 4). At the time of bar formation ( $z_{\text{bf}} \sim 2$ ) and until  $z \approx 0.5$ , the galaxies in the WW model have bulge-to-disc size ratios that are less than 0.5 and their  $B/D$  values are less than 0.3. This suggests the disc is still capable of forming a bar even though the galaxies in the WW model have concentrated bulges. At low redshift ( $z < 0.5$ ), the bulge continues to grow, but the bar length does not increase to the same extent as in the TNG50-like and BH variations models. This may suggest that the bulge could be influencing bar evolution. In contrast, the medium (MW) and strong (SW) wind models exhibit galaxies that show similar behaviour to those in the TNG50-like model, with  $B/D < 0.3$  at low redshift. The galaxies present higher  $B/D > 0.3$ , and the bulge-to-disc size ratio takes values higher than 0.5 at higher redshift. However, the discs are stable against bar formation in the first place.

## 5.2. What is the impact of feedback processes in bar formation?

As seen in section 3, feedback processes regulate star formation and affect the galaxies build-up and their components. In particular, they affect the mass of the disc, its size, and its kinematic

properties, such as radial velocity dispersion. These properties are tightly related to the trigger of bar instabilities. In particular, we found that for most of the cases, the models studied satisfy the ELN, MMW criteria for being stable/unstable discs and the Toomre and the Swing parameters at the time of bar formation, except for the no wind model and the weaker wind model, for which at least one of these criteria is not satisfied. The ELN and MMW criteria, in particular, indicate that the disc in the no wind model is susceptible to bar formation. Nevertheless, the Toomre parameter, which exhibits high values as a result of the presence of a concentrated bulge and high radial velocity dispersions, was able to explain that no stable bar was formed. The swing parameter has values in the unstable region, as demonstrated in 5, and the other two properties, high stellar surface density and higher epicyclic frequency, are not contributing factors in these cases. Conversely, in the case of galaxies in the weak wind model, the ELN and MMW criteria predict that the disc is unstable, and indeed, there is a strong but short bar. However, the Toomre parameter predicts high values due to the high radial velocity dispersion, as seen in the no wind model. It is important to note that the ELN and MMW do not consider a central concentration, strong random motions in the disc and halo or both components that could affect the conditions of bar formation (Athanasoula 2008) and it is possible that this is one of the reasons the ELN and MMW could not be satisfied. We also note that the galaxies with weak or no-SN feedback are not realistic, and we have only studied them to gain an understanding of the effects of feedback processes on bar formation, but we already know that these models predict galaxies that overestimate the baryon content of galaxies (see Pillepich et al., 2018a). Our findings suggest that the formation of bars may serve as a constraint on the subgrid feedback models of galaxy formation, thereby contributing significantly to our understanding of galaxy evolution.



### 5.3. What is the effect of stochasticity of feedback processes in bar formation

Something to be aware of when trying to understand our results is to take into account the stochasticity provided by sub-grid physics in simulations. In particular, Genel et al. (2019) found that simulations with feedback mechanisms could exhibit a stronger butterfly effect than those without feedback. This suggests that the dynamics at galactic scales could significantly influence how small differences in initial conditions can evolve into larger discrepancies in galaxy properties (see also Borrow et al. 2023 for other galaxy formation models). It is essential to acknowledge that the morphology of the models under investigation here is not significantly affected; however, the radial velocity dispersion and the extent of the disc could be. These qualities are employed to determine the stability of a disc, as seen in Figs. 4 & 8. The TNG50 simulation predicted the presence of six strongly barred galaxies; however, only five of these galaxies present a strong bar in the TNG50-like model at  $z = 0$ . The galaxy that does not present a bar, in the original TNG50, this bar was the weakest. In the TNG50-like model, it forms a bar at a time, similar to the one in the original TNG50. However, the bar formed weakens in time, probably because the black hole is less massive and the energy released in radio mode is smaller, increasing the gas fraction in the centre. This is an example, but in general, minor variations in the characteristics of bars appear to be associated with this stochasticity. On the other hand, when the feedback mechanisms differ, the merging histories are very similar to the original TNG50. The stochastic uncertainty that is incorporated into simulations limits the physical conclusions that can be derived. The broad causal tendencies we have identified suggest that this constraint is of lesser significance. However, it is necessary to study in more detail and with a larger statistical sample.

### 5.4. Outlook

The zoom-in hydrodynamic simulations have enabled us to investigate the influence of feedback processes with the advantage of previous works using TNG50 simulation. We resimulate six Milky-Way like galaxies from the TNG50 simulations. These galaxies have a stable galactic bar at  $z = 0$  which was formed between  $z = 3$  and  $z = 1.5$  (more than 8 giga years ago) and with quiet merger histories and isolated haloes. Even so, it is crucial to recognise the limitations of this investigation. The physics above scales of approximately 288 pc can be resolved by these zoom-ins. Although this is sufficient for a comprehensive examination of the formation and evolution of bars within the most massive galaxies in the local universe, simulations with a higher resolution are required to correctly track the initial phases of bar build-up at high redshifts. Recent observations from JWST have shown that bars exist at high redshifts (Guo et al. 2023; Costantin et al. 2023; Guo et al. 2024). The conditions which galaxies are subject to at such high redshifts are notably distinct from lower redshifts. It is anticipated that the frequency of encounters and mergers is higher (Bi, Shlosman, & Romano-Díaz 2022a,b) at such early times. A cosmological context would be an interesting setting in which to conduct this experiment with an extensive statistical galaxy sample and in different environments at higher redshift.

It is thought that bars drive flows into the galaxy centre, which in turn affects central star formation or the accretion onto the supermassive black hole (e.g., Fanali et al. 2015; Spinoso et al. 2017). The fate of the gas in the nuclear zone, affected by

the bar and other physical processes like SN and AGN feedback, should be studied. In particular, it would be interesting to see gaseous bars formed by stellar bar torques (Englmaier & Shlosman 2004).

The effects of the star formation processes on the bar properties, especially the bar pattern speed, which is the least constraint, need to be studied. The bar pattern speed is most affected by the interaction between the bar, disc, and the central dark matter distribution (Cuomo et al. 2020). The main effect is a slow-down of the bar as a function of time. This seems to be in contradiction with observations, which have found that bar pattern speeds are rapid. Using the zoom-in simulations, we can see the effect of the star formation processes at high redshift that affect the initial bar pattern speed when the bar forms (Semczuk et al. 2024).

## 6. Summary

In this work, we investigate the impact of feedback processes on the formation and evolution of bars in galaxies similar to the Milky Way. We study a suite of zoom-in cosmological hydrodynamical simulations of Milky Way-sized haloes selected from the TNG50 simulations in which the original galaxies form a strong bar between  $z = 1.5$  and  $z = 3$ . In particular, we explore variations of the supernova (SN) feedback and black hole (BH) physics models within the TNG galaxy formation model. Specifically, our investigation focuses on five different intensity levels within the galactic wind models (energy injected into the galactic wind per SN event) and two models of black hole physics affecting the AGN feedback in the quasar mode regime.

The results of our investigation are as follows:

- Our analysis revealed that the feedback from SN impacts the formation of a bar, while the effect of changing the modelling of BH physics in the quasar mode on its formation is negligible (Figs. 1 & 3). However, BH physics can affect the ultimate characteristics of a bar, such as strength and length. In order to gain a deeper understanding, we examine the characteristics of the various components of the galaxy.
- It was observed that the morphology at low redshift remained consistent in the sense that in all the models, galaxies developed a massive disc ( $> 10^{10}M_{\odot}$ ), which is dominant in comparison with the bulge mass (Fig. 3).
- Our findings indicate that SN feedback has a significant impact not only on the stellar mass content but also on the structural properties of the disc and bulge, including the disc size, thickness, and bulge size (see Table 3 & Fig. 4). SN feedback also affects the formation time of the disc and bulge, and then bar formation, which aligns with the finding by Zana et al. (2019). In extreme cases where the SN feedback is strong, bar formation is stopped. Our analysis revealed that the bulge and disc in galaxies lacking SN feedback is noticeably more compact and concentrated than those with stronger feedback at  $z = 0$ . In such galaxies, bar formation also stops.
- Based on these findings, it is evident that the feedback from supernovae plays a crucial role in shaping the various components found within galaxies. When the feedback strength is increased, it causes a decrease in the rate at which the disc grows. As a result, this affects the (thin) disc and bulge characteristics. The models varying BH physics in quasar mode do not influence the disc or the bulge formation, as also seen in Irodou et al. (2022) using the Auriga simulations.
- We thoroughly review the bar instability criteria in our different models, in particular during the process of bar formation.

Specifically, we focus on three criteria: the Toomre 1964, Efstathiou, Lake & Negroponete (1982, ELN), and Mo, Mao, & White (1998, MMW) criteria. Our analysis revealed that the sizes of the discs (Fig. 4), the stellar mass of the disc over halo mass (Fig. 7) and the radial velocity dispersion (Fig. 8) are strongly influenced by SN feedback and used to determine if a disc is prone to instability and bar formation (Fig. 5). Most of the models satisfy the instability criteria at the moment of bar formation, as in the barred galaxies in TNG50 (Izquierdo-Villalba et al. 2022). The exception is the no wind model, which presents higher radial velocity dispersion leading to high values of the Toomre parameter, whereas the ELT and MMW criteria predict an unstable disc.

- In galaxies in the weak winds and TNG50-like models, discs exhibit instability and give rise to bar formation, while galaxies in the strong and medium wind models do not form a bar. On the other hand, galaxies in the no wind model do not form a bar even though the disc satisfies some instability criteria. This could be explained by the presence of a massive and compact bulge (see Fig. 9). This is in agreement with Kataria & Das (2018), which found that galaxies with  $B/D > 0.3$  for concentrated bulges ( $B/D > 0.6$  for less concentrated bulges) prevent bar formation.

The comparison of galaxy formation models in our study offers a deeper understanding of the relationship between the emergent structures of galaxies and the input physics assumptions during their formation and evolution. This understanding could inspire new approaches to the prescription of galaxy formation models, offering hope for further advancements in the field.

Our research can also be employed to evaluate the predictive capabilities of analytics methods employed to identify the presence of a bar. This would enhance our comprehension of bar formation and enhance the modelling of barred galaxies in more empirical models.

*Acknowledgements.* The authors thank Volker Springel for providing them with the AREPO code and the TNG model and his suggestions regarding the project. The authors thankfully acknowledge the computer resources at MareNostrum and the technical support provided by Barcelona Supercomputing Center (RES-AECT-2023-2-0015). YRG acknowledges the support of the “Juan de la Cierva Incorporation” Fellowship (IJC2019-041131-I). S.B. & YRG acknowledge support from the Spanish Ministerio de Ciencia e Innovación through project PID2021-124243NB-C21. SC acknowledges the support of the ‘Juan de la Cierva Incorporación’ fellowship (IJC2020-045705-I). S.B., SC & YRG acknowledge support from the European Research Executive Agency HORIZON-MSCA-2021-SE-01 Research and Innovation programme under the Marie Skłodowska-Curie grant agreement number 101086388 (LACEGAL). Technical and human support provided by DIPC Supercomputing Center is gratefully acknowledged.

## References

Algorry D. G., et al., 2017, MNRAS, 469, 1054  
 Aricò G., Angulo R. E., Hernández-Monteaugado C., Contreras S., Zennaro M., 2021, MNRAS, 503, 3596.  
 Athanassoula E., Misiriotis A., 2002, MNRAS, 330, 35  
 Athanassoula E. 2003, MNRAS, 341, 1179 (A03)  
 Athanassoula E., 2008, MNRAS, 390, L69.  
 Athanassoula E., Machado R. E. G., Rodionov S. A., 2013, MNRAS, 429, 1949  
 Bi D., Shlosman I., Romano-Díaz E., 2022, MNRAS, 513, 693.  
 Bi D., Shlosman I., Romano-Díaz E., 2022, ApJ, 934, 52.  
 Binney J., Tremaine S., 2008, *gady.book*  
 Bird S., Vogelsberger M., Haehnelt M., Sijacki D., Genel S., Torrey P., Springel V., et al., 2014, MNRAS, 445, 2313.  
 Bonoli S., Mayer L., Kazantzidis S., Madau P., Bellovary J., Governato F., 2016, MNRAS, 459, 2603  
 Bower R. G., Benson A. J., Malbon R., Helly J. C., Frenk C. S., Baugh C. M., Cole S., Lacey C. G., 2006, MNRAS, 370, 645.

Borrow J., Schaller M., Bahé Y. M., Schaye J., Ludlow A. D., Ploekinger S., Nobels F. S. J., et al., 2023, MNRAS, 526, 2441.  
 Bullock J. S., Dekel A., Kolatt T. S., Kravtsov A. V., Klypin A. A., Porciani C., Primack J. R., 2001, ApJ, 555, 240.  
 Cervantes Sodi B., Li C., Park C., 2015, ApJ, 807, 111  
 Cervantes Sodi B., 2017, ApJ, 835, 80  
 Collier A., Shlosman I., Heller C., 2018, MNRAS, 476, 1331.  
 Costantin L., Pérez-González P. G., Guo Y., Buttitta C., Jooe S., Bagley M. B., Barro G., et al., 2023, Natur, 623, 499  
 Crain R. A., van de Voort F., 2023, ARA&A, 61, 473.  
 Croton D. J., Springel V., White S. D. M., De Lucia G., Frenk S. C., Gao L., Jenkins A. and Kauffmann G. et al., 2006, MNRAS, 365, 11.  
 Cuomo V., Aguerri J. A. L., Corsini E. M., Debattista V. P., 2020, A&A, 641, A111.  
 Dahari O., 1984, The Astronomical Journal, 89, 966  
 Debattista V. P., Mayer L., Carollo C. M., Moore B., Wadsley J., Quinn T., 2006, ApJ, 645, 209  
 Di Matteo T., Springel V., Hernquist L., 2005, Natur, 433, 604  
 Donohoe-Keyes C. E., Martig M., James P. A., Kraljic K., 2019, arXiv, arXiv:1908.11119  
 Efstathiou G., Lake G., Negroponete J., 1982, MNRAS, 199, 1069  
 Englmaier P., Shlosman I., 2004, ApJL, 617, L115.  
 Fanali R., Dotti M., Fiacconi D., Haardt F., 2015, MNRAS, 454, 3641  
 Fragkoudi F., Grand R. J. J., Pakmor R., Blázquez-Calero G., Gargiulo I., Gomez F., Marinacci F., et al., 2020, MNRAS, 494, 5936.  
 Fragkoudi F., Grand R., Pakmor R., Gómez F., Marinacci F., Springel V., 2024, arXiv, arXiv:2406.09453.  
 Fraser-McKelvie A., Merrifield M., Aragón-Salamanca A., Peterken T., Kraljic K., Masters K., Stark D., et al., 2020, MNRAS, 499, 1116.  
 Faucher-Giguère C.-A., Lidz A., Zaldarriaga M., Hernquist L., 2009, ApJ, 703, 1416  
 Gadotti D. A., 2009, MNRAS, 393, 1531  
 Gavazzi G., et al., 2015, A&A, 580, A116  
 Genel S., et al., 2014, MNRAS, 445, 175  
 Genel S., Bryan G. L., Springel V., Hernquist L., Nelson D., Pillepich A., Weinberger R., et al., 2019, ApJ, 871, 21  
 George K., Subramanian S., Paul K. T., 2019, arXiv, arXiv:1907.06910  
 Ghosh S., Fragkoudi F., Di Matteo P., Saha K., 2023, A&A, 674, A128.  
 Guedes J., Callegari S., Madau P., Mayer L., 2011, ApJ, 742, 76  
 Guo Y., Jooe S., Finkelstein S. L., Chen Z., Wise E., Bagley M. B., Barro G., et al., 2023, ApJL, 945, L10.  
 Guo Y., Jooe S., Wise E., Pritchett K., McGrath E. J., Finkelstein S. L., Iyer K. G., et al., 2024,  
 Grand R. J. J., Gómez F. A., Marinacci F., Pakmor R., Springel V., Campbell D. J. R., Frenk C. S., et al., 2017, MNRAS, 467, 179.  
 Henriques B. M. B., White S. D. M., Thomas P. A., Angulo R. E., Guo Q., Lemson G., Springel V., 2013, MNRAS, 431, 3373.  
 Irodoutou D., Fragkoudi F., Pakmor R., Grand R. J. J., Gadotti D. A., Costa T., Springel V., et al., 2022, MNRAS, 513, 3768.  
 Izquierdo-Villalba D., Bonoli S., Rosas-Guevara Y., Springel V., White S. D. M., Zana T., Dotti M., et al., 2022, arXiv, arXiv:2203.07734  
 Joshi G. D., Pontzen A., Agertz O., Rey M. P., Read J., Pillepich A., 2024, arXiv, arXiv:2407.00171.  
 Kataria S. K., Das M., 2018, MNRAS, 475, 1653  
 Katz N., Weinberg D. H., Hernquist L., 1996, ApJS, 105, 19  
 Le Conte Z. A., Gadotti D. A., Ferreira L., Conselice C. J., de Sá-Freitas C., Kim T., Neumann J., et al., 2023, arXiv, arXiv:2309.10038  
 Kraljic K., Bournaud F., Martig M., 2012, ApJ, 757, 60  
 Long S., Shlosman I., Heller C., 2014, ApJL, 783, L18  
 Marinacci F., et al., 2018, MNRAS, 480, 5113  
 Masters K. L., et al., 2011, MNRAS, 411, 2026  
 Mo H. J., Mao S., White S. D. M., 1998, MNRAS, 295, 319.  
 Naiman J. P., et al., 2018, MNRAS, 477, 1206  
 Navarro J. F., Benz W., 1991, ApJ, 380, 320.  
 Nelson D., et al., 2015, A&C, 13, 12  
 Nelson D., et al., 2018a, MNRAS, 475, 624  
 Nelson D., et al., 2019a, ComAC, 6, 2  
 Nelson D., Pillepich A., Springel V., Pakmor R., Weinberger R., Genel S., Torrey P., et al., 2019b, MNRAS, 490, 3234.  
 Oppenheimer B. D., Davé R., 2006, MNRAS, 373, 1265.  
 Oppenheimer B. D., Davé R., 2008, MNRAS, 387, 577.  
 Ostriker J. P., Peebles P. J. E., 1973, ApJ, 186, 467  
 Peschken N., Łokas E. L., 2019, MNRAS, 483, 2721  
 Pillepich A., et al., 2018a, MNRAS, 473, 4077  
 Pillepich A., et al., 2018b, MNRAS, 475, 648  
 Pillepich A., Nelson D., Springel V., Pakmor R., Torrey P., Weinberger R., Vogelsberger M., et al., 2019, MNRAS, 490, 3196  
 Pillepich A., Sotillo-Ramos D., Ramesh R., Nelson D., Engler C., Rodriguez-Gomez V., Fournier M., et al., 2023, arXiv, arXiv:2303.16217.  
 Planck Collaboration 2016, A&A, 594, A13

- Pontzen A., Governato F., 2012, *MNRAS*, 421, 3464.
- Rodriguez-Gomez V., et al., 2015, *MNRAS*, 449, 49
- Romeo A. B., Agertz O., Renaud F., 2023, *MNRAS*, 518, 1002.
- Rosito M. S., Tissera P. B., Pedrosa S. E., Rosas-Guevara Y., 2019, *A&A*, 629, A37.
- Rosas-Guevara Y., Bonoli S., Dotti M., Zana T., Nelson D., Pillepich A., Ho L. C., et al., 2020, *MNRAS*, 491, 2547
- Rosas-Guevara Y., Bonoli S., Dotti M., Izquierdo-Villalba D., Lupi A., Zana T., Bonetti M., et al., 2022, *MNRAS*, 512, 5339
- Saha K., Naab T., 2013, *MNRAS*, 434, 1287.
- Saha K., Elmegreen B., 2018, *ApJ*, 858, 24.
- Scannapieco C., Athanassoula E., 2012, *MNRAS*, 425, L10
- Schaye J., et al., 2015, *MNRAS*, 446, 521
- Sellwood J. A., Wilkinson A., 1993, *RPPh*, 56, 173
- Sellwood J. A., 2012, *ApJ*, 751, 44.
- Sheth K., Melbourne J., Elmegreen D. M., Elmegreen B. G., Athanassoula E., Abraham R. G., Weiner B. J., 2012, *ApJ*, 758, 136
- Sijacki D., et al., 2015, *MNRAS*, 452, 575
- Semczuk M., Dehnen W., Schönrich R., Athanassoula E., 2024, *arXiv*, arXiv:2407.11154.
- Spinoso D., Bonoli S., Dotti M., Mayer L., Madau P., Bellovary J., 2017, *MNRAS*, 465, 3729
- Springel V., White S. D. M., Tormen G., Kauffmann G., 2001, *MNRAS*, 328, 726
- Springel V., Hernquist L., 2003, *MNRAS*, 339, 289
- Springel V., Di Matteo T., Hernquist L., 2005, *MNRAS*, 361, 776
- Springel V., 2010, *MNRAS*, 401, 791
- Springel V., 2015, *ascl.soft.ascl:1502.003*
- Springel V., et al., 2018, *MNRAS*, 475, 676
- Suresh J., Bird S., Vogelsberger M., Genel S., Torrey P., Sijacki D., Springel V., et al., 2015, *MNRAS*, 448, 895.
- Toomre A., 1964, *ApJ*, 139, 1217.
- Vogelsberger M., Genel S., Sijacki D., Torrey P., Springel V., Hernquist L., 2013, *MNRAS*, 436, 3031
- Vogelsberger M., et al., 2014a, *Nature*, 509, 177
- Vogelsberger M., et al., 2014b, *MNRAS*, 444, 1518
- Vogelsberger M., Marinacci F., Torrey P., Puchwein E., 2020, *NatRP*, 2, 42.
- Weinberger R., et al., 2017, *MNRAS*, 465, 3291
- Yurin D., Springel V., 2015, *MNRAS*, 452, 2367.
- Zana T., Dotti M., Capelo P. R., Bonoli S., Haardt F., Mayer L., Spinoso D., 2018a, *MNRAS*, 473, 2608
- Zana T., et al., 2019, *MNRAS*, 488, 1864
- Zana T., Lupi A., Bonetti M., Dotti M., Rosas-Guevara Y., Izquierdo-Villalba D., Bonoli S., et al., 2022, *MNRAS*, 515, 1524.
- Zhao D., Du M., Ho L. C., Debattista V. P., Shi J., 2020, *ApJ*, 904, 170
- Zhou Z.-B., Zhu W., Wang Y., Feng L.-L., 2020, *ApJ*, 895, 92.

## Appendix A: Kinematic decomposition and bar identification

In order to identify more precise galaxy components, we adopt the kinematic decomposition algorithm `MORDOR`<sup>3</sup> presented in Zana et al. (2022) to determine more specific galaxy components. The decomposition is predicated on the circularity ( $\epsilon$ ) and binding energy ( $E$ ) phase space, where a minimum in  $E$  is identified for each galaxy,  $E_{\text{cut}}$ . All four components listed below were identified for the simulations employed in the paper:

- **Classical Bulge:** is defined as the set of stellar particles that exhibit the highest degree of binding, with a value that is contingent upon the  $E_{\text{cut}}$  of each galaxy. These particles also exhibit counterrotation, which is characterised by a negative value of  $\epsilon$  ( $\epsilon < 0$ ). Next, Monte Carlo sampling is employed to select a distribution that is equivalent to the component of the distribution that exhibits positive circularity and allocate it to the Bulge.
- **Thin/Cold disc:** is defined as the set of stellar particles that have the highest degree of binding and are not allocated to the Bulge, but have positive values of  $\epsilon$  ( $\epsilon > 0.7$ ).
- **Pseudobulge:** is defined as the remaining stellar particles that exhibit a high degree of binding without being assigned to the Bulge or the thin disc.
- **Thick/Warm disc:** is defined as the set of stellar particles that have positive  $\epsilon$  values ( $\epsilon > 0.7$ ) and are not assigned to the bulge/pseudobulge, despite exhibiting a reduced degree of binding.

The stellar density maps components of a galaxy are illustrated in Fig. A.1 for the TNG50-like model, in which the galaxy forms a bar, and for the strong wind model, in which the galaxy does not form a bar. `MORDOR` is employed to generate these maps. The distinctions between all of the components are readily apparent. For this example, the thick disc seems to trace the bar, while the pseudobulge appears to be indistinguishable from the bulge. This also seems to be the case at the time of bar formation.

### Appendix A.1: Identification of bars

The face-on stellar surface density is Fourier decomposed to identify non-axisymmetric structures (e.g., Athanassoula & Misiriotis 2002; Zana et al. 2018a; Rosas-Guevara et al. 2020). We concentrate on  $A_2(R)$ , which is defined by the ratio between the second and zero terms of the Fourier expansion and its phase  $\Phi(R)$  (refer to equations 1 and 2 in RG22). A bar structure is characterised by  $A_2(R)$  and  $\Phi(R)$ , with the bar strength defined as  $A_{2,\text{max}}$ , the peak of  $A_2(R)$ . Inside the bar, the phase should be constant. To establish a constant phase, we calculate the standard deviation ( $\sigma$ ) of  $\Phi(R)$  every time a new cylinder shell is added and set  $\sigma \leq 0.1$ . The bar extent ( $r_{\text{bar}}$ ) is the greatest radius where  $\sigma \leq 0.1$ , and the  $A_2$  profile first dips below 0.15 or the minimum value of  $A_2(R)$ . Large values of  $A_2(R)$  may be attributable to transient events like mergers and interactions; thus, we assume the bar represents a long-lasting characteristic if

1. The maximum of  $A_2$ ,  $A_{2,\text{max}}$ , is greater than 0.2,
2.  $r_{\text{bar}} > r_{\text{min}}$  where  $r_{\text{min}} = 1.38 \times \epsilon_{*,z}$  is a minimum radius imposed and  $\epsilon_{*,z}$  corresponds to the proper softening length for stellar particles.
3. The estimated age of the bar is larger than the time between the analysed output and 2 previous simulation outputs.

Although this filter may omit newer bars at lower redshifts, it aligns with the bar selection criteria employed by RG20; RG22 when bar structure was found in previous outputs.

To identify a bar structure, the formation time,  $t_{\text{bar}}$ , must also be determined. We follow the growth of  $A_{2,\text{max}}$  up to the moment when  $A_{2,\text{max}} \leq 0.2$  and  $r_{\text{bar}}(t_{\text{bar}}) \leq r_{\text{min}}$  for several snapshots. Additionally, the difference between  $A_{2,\text{max}}$  at a snapshot and the two prior snapshots must not exceed 0.45 during this time frame. This confirms that the bars we find are stable.

### Appendix A.2: Method of three-component decomposition of surface face-on density profile

In this section, we outline the process of decomposing the surface brightness profiles of the galaxies to determine the length scale of the disc, the effective radius of the bulge, and the properties of the bar when it is identified through Fourier decomposition. The surface density profiles are calculated in a face-on perspective within concentric annuli that are 0.16 dex in width and centred on the stellar component minimal potential.

We employ the particle swarm optimisation (PSO) code `PSOBacco`<sup>4</sup> (Aricò et al. 2021) to determine the minimum  $\chi^2$  of a fit of the sum of an exponential profile and two Sersic profiles (one of which corresponds to the bar). This value is expressed in terms of the stellar mass as

$$\Sigma(R) = \Sigma_{\text{d},0} \exp\left(-R/h_{\text{disc},*}\right) + \Sigma_{\text{b},e} \exp\left(-b_n \left[(r/r_{\text{b,eff}})^{1/n} - 1\right]\right) + \Sigma_{\text{bar},e} \exp\left(-b_n \left[(r/r_{\text{bar,eff}})^{1/n_{\text{bar}}} - 1\right]\right) \quad (\text{A.1})$$

where  $\Sigma_{\text{d},0}$  is the central surface density of the disc component,  $h_{\text{disc},*}$  is the disc scale length,  $r_{\text{b,eff}}$  ( $r_{\text{bar}}$ ) the effective radius that encloses half of the stellar mass of the one predicted from the Sersic profile,  $\Sigma_{\text{b},e}$  ( $\Sigma_{\text{bar},e}$ ) corresponds to the surface density at  $r_{\text{b,eff}}$ , and  $n$  is the Sersic index (of the bulge/bar). The value of  $b_n$  is contingent upon the complete gamma function, as  $\Gamma(2n) = 2\gamma(2n, b_n)$ .

We apply the method of fitting three components in the region at radii smaller than  $r_{\text{fit}} = \max(\log_{10}(\Sigma(r)/\Sigma_{\text{max}}) \geq -2.6, 10 \text{ kpc})$  when a bar is detected by Fourier decomposition. If not, we fit two components. This condition guarantees to suit both high-redshift discs, which are more compact (smaller disc scale lengths for a given stellar mass), and their analogues at low redshifts, whose discs are less compact (larger disc scale lengths for a given stellar mass).

The surface density profiles and the fits for a galaxy in the TNG50-like model, where a bar is formed, and the same galaxy in the strong wind model, where a bar is not formed, are illustrated in Fig. A.2. A black line denotes the total fitted profile. The disc, bar, and bulge components are represented by blue, pink, and red lines, correspondingly. As a point of reference, the scale-length of a disc,  $h_{\text{disc},*}$ , the effective radius of the bulge,  $r_{\text{b,eff}}$ , and the length of the bar in the case of barred galaxies are represented by coloured vertical lines. The vertical lines that are dashed represent the radius at which the fit is performed.

<sup>3</sup> <https://github.com/thanatom/mordor>

<sup>4</sup> [https://github.com/hantke/pso\\_bacco](https://github.com/hantke/pso_bacco)

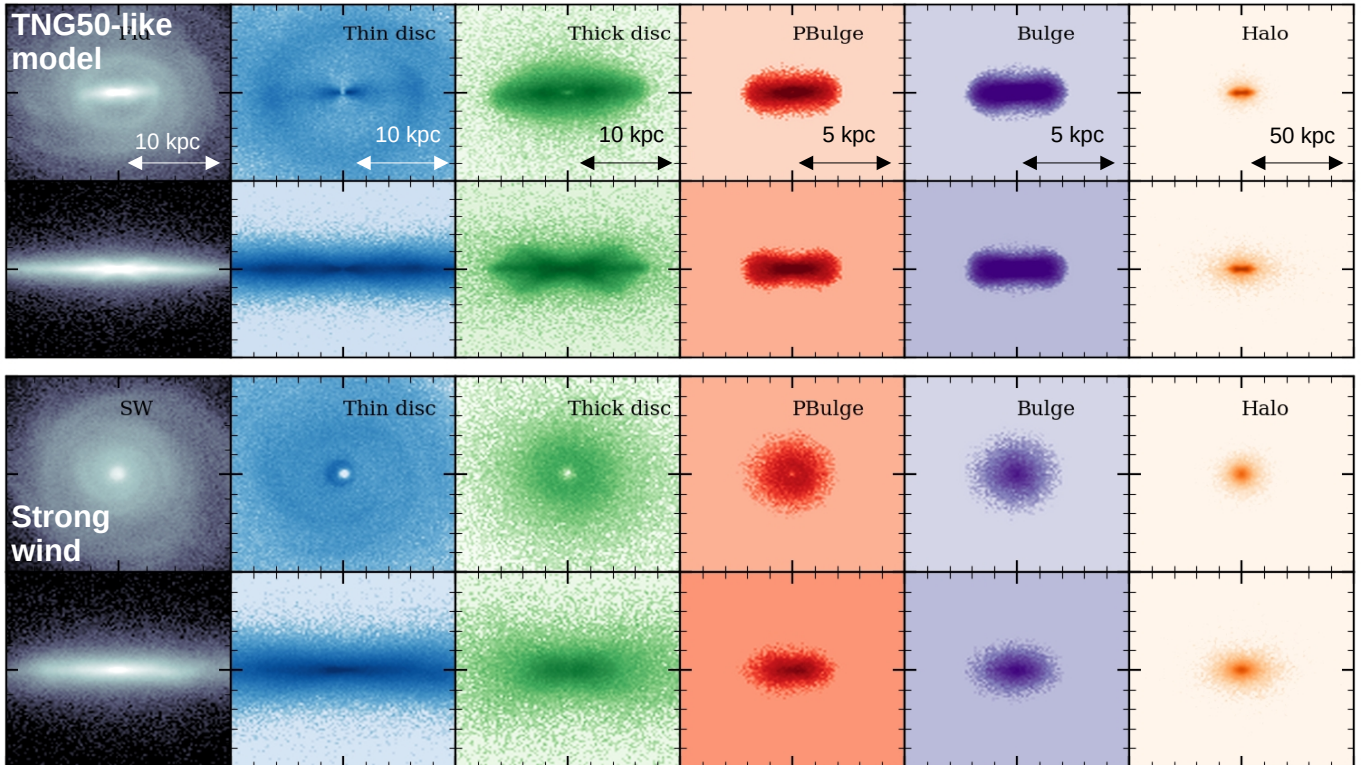


**Fig. A.1.** Stellar density maps of the different galaxy components identified by MORDOR. From left to right columns: total galaxy, thin disc, thick disc, Pseudobulge, bulge, and halo. The top panels correspond to a galaxy in the TNG50-like model, and the bottom panel to the same galaxy in the strong wind model.

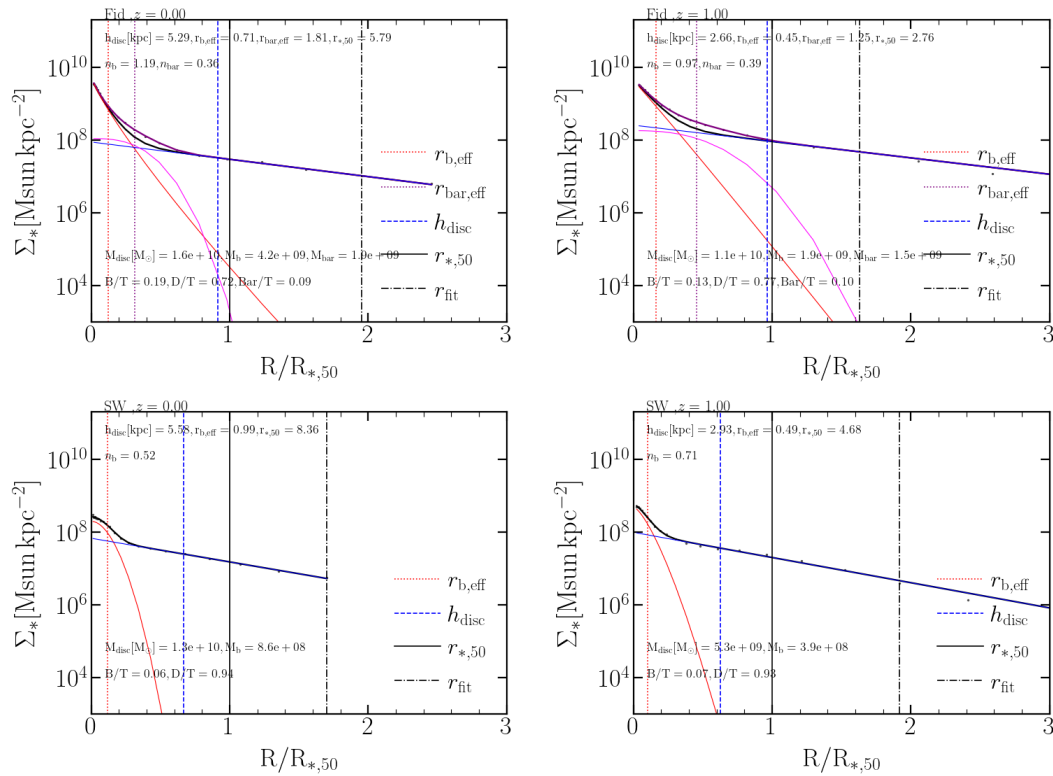


**Fig. A.2.** Examples of face-on stellar surface density profiles in terms of  $R/R_{*,50}$  where  $R_{*,50}$  is the stellar half-mass radius, for a galaxy with a bar in the TNG50-like model (top panels) and unbarred galaxy in the strong wind model (bottom panels) at  $z = 1, 0$ . The profiles (black lines) were obtained by fitting simultaneously a Sersic profile for a bulge (red lines) and a Sersic for a bar (pink lines), and an exponential profile (blue lines). Purple lines represent the surface density profile from the predicted Sersic profile and exponential profile. Horizontal dashed lines correspond to the radius at which the fit is done. Dotted horizontal lines correspond to the bar length (pink), the effective radius of the bulge (red), and the scale length of the disc (blue).